



NAVAL POSTGRADUATE SCHOOL

MONTEREY, CALIFORNIA

DISSERTATION

**ENHANCING MICROBOLOMETER PERFORMANCE AT
TERAHERTZ FREQUENCIES WITH METAMATERIAL
ABSORBERS**

by

Brian T. Kearney

September 2013

Dissertation Supervisor:

Gamani Karunasiri

Approved for public release; distribution is unlimited

THIS PAGE INTENTIONALLY LEFT BLANK

REPORT DOCUMENTATION PAGE			<i>Form Approved OMB No. 0704-0188</i>	
Public reporting burden for this collection of information is estimated to average 1 hour per response, including the time for reviewing instruction, searching existing data sources, gathering and maintaining the data needed, and completing and reviewing the collection of information. Send comments regarding this burden estimate or any other aspect of this collection of information, including suggestions for reducing this burden, to Washington headquarters Services, Directorate for Information Operations and Reports, 1215 Jefferson Davis Highway, Suite 1204, Arlington, VA 22202-4302, and to the Office of Management and Budget, Paperwork Reduction Project (0704-0188) Washington DC 20503.				
1. AGENCY USE ONLY (Leave blank)		2. REPORT DATE September 2013	3. REPORT TYPE AND DATES COVERED Dissertation	
4. TITLE AND SUBTITLE ENHANCING MICROBOLOMETER PERFORMANCE AT TERAHERTZ FREQUENCIES WITH METAMATERIAL ABSORBERS			5. FUNDING NUMBERS	
6. AUTHOR(S) Brian T. Kearney				
7. PERFORMING ORGANIZATION NAME(S) AND ADDRESS(ES) Naval Postgraduate School Monterey, CA 93943-5000			8. PERFORMING ORGANIZATION REPORT NUMBER	
9. SPONSORING /MONITORING AGENCY NAME(S) AND ADDRESS(ES) N/A			10. SPONSORING/MONITORING AGENCY REPORT NUMBER	
11. SUPPLEMENTARY NOTES The views expressed in this thesis are those of the author and do not reflect the official policy or position of the Department of Defense or the U.S. Government. IRB Protocol number ____ N/A ____.				
12a. DISTRIBUTION / AVAILABILITY STATEMENT Approved for public release; distribution is unlimited			12b. DISTRIBUTION CODE	
13. ABSTRACT (maximum 200 words) For Terahertz (THz) imaging to be useful outside of a laboratory setting, inexpensive yet sensitive detectors such as uncooled microbolometers will be required. Metamaterials can improve THz absorption without significantly increasing the thermal mass or using exotic materials because their absorption is primarily dependent on the geometry of the materials and not their individual optical properties. Finite Element (FE) simulations revealed that an array of squares above a ground plane separated by a dielectric is efficient, yet thin. Metamaterials were fabricated and their absorption characteristics were measured using a Fourier Transform Infrared Spectrometer (FTIR) indicating that the FE simulations are accurate. Metamaterial structures tuned to a quantum cascade laser (QCL) illuminator were incorporated into a bi-material sensor, which was used for detection of THz radiation from the QCL source with good sensitivity. In the case of microbolometers, a bolometric layer needs to be embedded in the metamaterial to form a thin microbridge. Simulations indicated that if the bolometric layer was resistive enough or close enough to the ground plane, then absorption would be largely unaltered. Metamaterials with a conductive Titanium (Ti) layer embedded into the dielectric spacer were fabricated and measured with an FTIR, confirming this behavior.				
14. SUBJECT TERMS Terahertz, Metamaterial, Perfect Absorber, Microbolometer, Thermal Imager, Bimaterial Sensor, Thin Film Absorber			15. NUMBER OF PAGES 89	
			16. PRICE CODE	
17. SECURITY CLASSIFICATION OF REPORT Unclassified	18. SECURITY CLASSIFICATION OF THIS PAGE Unclassified	19. SECURITY CLASSIFICATION OF ABSTRACT Unclassified	20. LIMITATION OF ABSTRACT UU	

THIS PAGE INTENTIONALLY LEFT BLANK

Approved for public release; distribution is unlimited

**ENHANCING MICROBOLOMETER PERFORMANCE AT TERAHERTZ
FREQUENCIES WITH METAMATERIAL ABSORBERS**

Brian T. Kearney
Civilian, Department of the Navy
B.A., University of California Berkeley, 2008

Submitted in partial fulfillment of the
requirements for the degree of

DOCTOR OF PHILOSOPHY IN APPLIED PHYSICS

from the

**NAVAL POSTGRADUATE SCHOOL
September 2013**

Author:

Brian T. Kearney

Approved by:

Gamani Karunasiri
Professor of Physics
Dissertation Supervisor

Andres Larraza
Associate Professor of Physics

Dragoslav Grbovic
Assistant Professor of Physics

James Luscombe
Professor of Physics

Todd Weatherford
Associate Professor of Electrical
& Computer Engineering

Approved by:

Andres Larraza, Chair, Department of Physics

Approved by:

Douglas Moses, Vice Provost for Academic Affairs

THIS PAGE INTENTIONALLY LEFT BLANK

ABSTRACT

For Terahertz (THz) imaging to be useful outside of a laboratory setting, inexpensive, yet sensitive, detectors such as uncooled microbolometers will be required. Metamaterials can improve THz absorption without significantly increasing the thermal mass or using exotic materials because their absorption is primarily dependent on the geometry of the materials and not their individual optical properties. Finite Element (FE) simulations revealed that an array of squares above a ground plane separated by a dielectric is efficient, yet thin. Metamaterials were fabricated and their absorption characteristics were measured using a Fourier Transform Infrared Spectrometer indicating that the FE simulations are accurate. Metamaterial structures tuned to a quantum cascade laser (QCL) illuminator were incorporated into a bi-material sensor, which was used for detection of THz radiation from the QCL source with good sensitivity. In the case of microbolometers, a bolometric layer needs to be embedded in the metamaterial to form a thin microbridge. Simulations indicated that if the bolometric layer was resistive enough or close enough to the ground plane, then absorption would be largely unaltered. Metamaterials with a conductive Titanium layer embedded into the dielectric spacer were fabricated and measured with an FTIR, confirming this behavior.

THIS PAGE INTENTIONALLY LEFT BLANK

TABLE OF CONTENTS

I.	INTRODUCTION.....	1
A.	TERAHERTZ IMAGING.....	1
B.	TERAHERTZ IMAGING USING UNCOOLED THERMAL DETECTORS.....	2
C.	OVERVIEW OF PRESENT RESEARCH.....	4
II.	METAMATERIAL ABSORBERS	9
A.	SIMULATION	10
B.	FABRICATION	15
C.	MEASUREMENT.....	17
D.	OPTIMIZATION AND TUNING OF SINGLE-BAND METAMATERIAL ABSORBERS	20
E.	OTHER METAMATERIAL CONFIGURATIONS AND EMISSION CHARACTERISTICS.....	23
III.	METAMATERIALS INTEGRATED INTO THERMAL SENSORS	31
A.	THERMAL SENSOR PROPERTIES	31
B.	BI-MATERIAL SENSOR CHARACTERISTICS	33
C.	BI-MATERIAL THZ SENSOR DESIGN	37
D.	FABRICATION AND CHARACTERIZATION	42
IV.	INTEGRATING METAMATERIALS INTO MICROBOLOMETER PIXELS	51
A.	CHALLENGES TO BOLOMETER INTEGRATION.....	51
B.	FABRICATION AND MEASUREMENT	51
C.	RESULTS AND DISCUSSION	54
D.	OTHER POSSIBLE CONFIGURATIONS	56
V.	CONCLUSION	59
A.	FUTURE WORK.....	60
	LIST OF REFERENCES.....	63
	INITIAL DISTRIBUTION LIST	69

THIS PAGE INTENTIONALLY LEFT BLANK

LIST OF FIGURES

Figure 1.	Electromagnetic spectrum showing the location of the terahertz band. From [2]	1
Figure 2.	Blackbody distributions for various temperatures with the THz band shaded in blue and IR in red. THz makes up only a small fraction of blackbody emission at common temperatures. From [20].....	3
Figure 3.	Knife covered in opaque white plastic tape (a) is visible in THz. Absorption (b) of a 1 μm thick Silicon Nitride membrane, showing poor absorption in THz. (b) From [20].	4
Figure 4.	Unit cell (a) of a metamaterial with a single absorption peak. The model also incorporates the unintentional over-etch into the SiO_x during the fabrication. Schematic representation (b) of the unit cell in the FE modeling program with boundary conditions and THz plane wave at normal incidence. Time-averaged power flow (c) near the resonant absorption frequency and arrow lengths relate to magnitude in log scale. From [23]	11
Figure 5.	Modeled absorption characteristics of the three layers of a metamaterial with single absorption peak. From [23]	14
Figure 6.	One of the fabricated wafers with 25 different metamaterials arranged radially for automated reflection measurements using a PIKE MappIR FTIR accessory. From [23]	17
Figure 7.	Raw FTIR data for a metamaterial absorber, showing the excessive noise in the spectral region below 3 THz.	18
Figure 8.	Schematic representation of the experimental configuration used for measuring the reflection (a) and transmission (b), before using the MappIR accessory. The accessory performs essentially the same measurements, but operates at an incident angle of 15 degrees. From [49]. ..	19
Figure 9.	FE model solution for 16 μm squares at the resonant absorption frequency. Electric (red) and magnetic (blue) fields for a metamaterial absorber at its resonant frequency. Note the opposing electric fields on either side of the square and the reversal of the magnetic field.....	20
Figure 10.	FTIR measurements (a) for varying square size, 21 μm pitch, and 1.47 μm SiO_x . Linear fit (b) of inverse square size ($1/s$) to resonant absorption frequency (ν). The effects of varying dielectric thickness (c) for 12 μm squares and 21 μm pitch and varying pitch (d) with 16 μm squares and 1.47 μm SiO_x . From [23]	21
Figure 11.	Simulations for 16 μm square size and 21 μm pitch with two dielectric thicknesses showing that for thicker cases, increasing periodicity can, in fact, increase percent absorption.....	23
Figure 12.	Unit cell (a) of a dual band metamaterial configuration. Measured (b) and modeled (c) absorption for a dual-band absorber with squares that have a 4 μm size difference compared to the same configuration with only one type of square. Comparison (d) of the absorption spectrum for dual band	

	absorber with 2 μm square size difference, overall pitch of 42 μm and SiO_x thickness 1.47 μm to a single band absorber with an intermediate square size. From [23].	24
Figure 13.	FE model solution for 16 and 18 μm squares at the resonant absorption frequency of the 18 μm squares (a) and the 16 μm squares (b). The center square is 18 μm . Electric (red) and magnetic (blue) fields are shown. Note how the 16 μm squares have a larger electric field in (a) than the 18 μm squares do in (b) showing that the 16 μm squares assist the 18 μm at their resonance, but not vice versa.	25
Figure 14.	Unit cell (a) and absorption characteristics (b) of a two peak metamaterial layer utilizing a tile configuration to maximize square density. From [23].	26
Figure 15.	Unit cell (a) and measured absorption (b) for a triple band metamaterial configuration with square sizes of 11, 14, and 17 μm showing three clear peaks. From [23].	27
Figure 16.	Measured emissivity of the metamaterial samples A, B and C at 400 $^\circ\text{C}$. Emissivity exhibits peaks at 4.1, 5.4 and 7.8 THz, respectively. From [24].	28
Figure 17.	Spectral absorptance of the metamaterial samples A, B and C. Solid lines represent the measured absorptance with peaks at 4.1, 5.4 and 7.8 THz, respectively. Dashed lines represent the finite element simulation results. From [24].	29
Figure 18.	Diagram showing heat exchange between a thermal sensor and its environment. Incoming power P creates a gradient of ΔT between the sensor and the heat sink at temperature T in addition to radiation losses. Convection losses are ignored as most sensors operate at low pressures. After [20].	31
Figure 19.	Responsivity (R_{th} [K/W]) vs thermal conductivity (G_{th} [W/K]) in a thermal sensor under sinusoidal illumination power. Clearly, regardless of G_{th} , R_{th} increases with higher absorption (η), lower frequencies (ω), and smaller C_{th} .	32
Figure 20.	Bi-material sensor. (a) 3D view of the THz bi-material sensor with integrated metamaterial absorber, fabricated on a Si substrate. (b) Close up of an isolated bi-material beam which length is l_b , and metal and dielectric thickness t_1 and t_2 , respectively. Δz_{leg} and $\Delta\theta$ are the linear and angular deflection of the beam, respectively. From [26].	35
Figure 21.	Thermomechanical deflection of the bi-material sensor. (a) Freestanding flat THz absorber connected to a bi-material beam, whose length is l_b , and metal and dielectric thickness t_1 and t_2 , respectively. Δz_{abs} is the total linear displacement and $\Delta\theta$ is the angular deflection of the absorber. (b) Thermomechanical sensitivity ($d\theta/dT$) of the structure of part (a), calculated using Equation (4) for all combinations of metal/dielectric of Table 1 where t_1 varies from 10 to 800 nm and t_2 is fixed in 1.1 μm . The circular marker shows FE and experimental results for $t_1 = 170$ nm. Solid lines are for Al combinations while dashed lines are for Au. From [26].	37
Figure 22.	Structural parameters of the three bi-material THz sensors in μm . (a) Top view of sensor A showing all dimensions. (b) Top view of sensors B and	

	C, showing the differences in sizes of the thermal insulator anchors. (c) Vertical cut of the sensor structure. From [26].	38
Figure 23.	FE simulations showing the deformation plots of sensor A (a), B (b) and C (c) under a constant $1 \mu\text{W}$ heat flux. The z-axes are scaled up 20 times for visual purposes. The surface colors indicate the temperature distribution according to the color bar on the left. (d) Time domain simulation of all three sensors under a $1 \mu\text{W}$ step excitation (black line). Temperature change and angular displacement are shown on the left and on the right, respectively. From [26].	41
Figure 24.	Fabricated THz bi-material sensors. (a) 3D optical profile of sensor A (the aspect ratio is preserved). (b) Micrograph of an array of sensor A. (c) 2D profile taken along the bimaterial legs direction (y-profile) with the processing direction (z-profile) scale exaggerated to show the residual deflection of the legs (red line) and absorber (blue line). (c) Micrographs showing the top view of sensors A, B and C. From [26].	43
Figure 25.	(a) Measurement of the absorptance spectra of the THz sensors metamaterial structure (blue line) compared with the QCL normalized emission (red line). (b) Measured angular deflection (markers) upon temperature change. Notice that the effect is linear and almost indistinguishable among the sensors, resulting in approximately 0.2 deg/K thermomechanical sensitivity. From [26].	44
Figure 26.	Responsivity and NEP measurements. (a) Measured angular deflection per varying incident power for all three sensors (colored markers) Notice that responsivity increases as thermal conductance decreases. (b) Measured output voltage of the PSD for sensor A by gating the QCL output at 200 mHz. The power incident in the detector is shown on the right vertical axis. From [26].	46
Figure 27.	Time and frequency domain measurements. (a) Time responses of sensors A, B and C measured under the same incident power with the QCL gated at 1 Hz. Noticed that sensor A is more sensitive and slower, which agrees with the predictions and previous measurements. (b) Normalized frequency responses for the three sensors (colored lines). The time constants were retrieved by taking the inverse of the 3 dB frequencies that are 1.2, 2.1 and 3.2 rad/s for sensor A, B and C, respectively. From [26].	47
Figure 28.	QCL beam imaging. (a) Optical readout used to record videos [46] and the snap shot showed in part (c). The images were recorded using background subtraction to suppress to the effects of the residual stress of the sensors. (b) Image obtained using a $30 \mu\text{m}$ pitch commercial IR microbolometer camera with THz optics. (c) Image (Media 1) of the same QCL beam, gated at 500 mHz, obtained using an array of sensor A with $430 \mu\text{m}$ pitch using the readout depicted in part (a). Notice that since the pitch of our sensor are one order of magnitude higher than the IR camera, it cannot resolve the rings associated with the QCL beam, showed in part (b). From [26].	49

Figure 29.	Schematic (a) and top view micrograph (b) of a metamaterial absorber with a bolometric layer embedded in the dielectric. The square size and pitch were selected to have an absorption peak within the 1–10 THz band. From [25].	52
Figure 30.	(a) Experimental (solid) and FE model (dashed) absorption spectra for samples A (black), B (red), and C (green). (b) Theoretical absorption curves for sample A for a set of sheet resistivities in the bolometric layer. Square size is 15 μm with 21 μm periodicity for both plots. From [25].	54
Figure 31.	E-field magnitude plots from COMSOL FE simulations of 15 μm squares with 21 μm pitch at 4.7 THz for samples A (a), B (b), and C (c). All plots use the same color scale, with warmer colors indicating more intense E-fields. Material types of different regions are labeled in (a). E-field, H-field, and propagation vectors of the incident THz waves are shown on (b). From [25].	55
Figure 32.	Three possible configurations for integrating a conductive layer into a THz absorbing metamaterial using a metal, bolometric layer, and a dielectric with the bolometric layer below (a) and within (c) the metamaterial layer. Configuration (c) thermally disconnects the ground plane. The configuration we used is shown in (b) with Ti.	57
Figure 33.	Wheatstone bridge configuration for THz metamaterial microbolometer characterization. The thermally shorted pixels are not released from the substrate and the blind pixel has a single metal square instead of the patterned layer and thus will not absorb THz efficiently, but will have essentially the same thermal properties as the sensitive pixel. Several Wheatstone bridges are fabricated together, their common ground is not visible.	61

LIST OF TABLES

Table 1.	Properties of standard MEMS materials[58], [59]. From [26].	36
Table 2.	THz bi-material sensor analytical, numerical, and experimental parameters. From [26].	39
Table 3.	Thickness of the dielectric spacer layers (in nm) of each sample. From [25].	53

THIS PAGE INTENTIONALLY LEFT BLANK

LIST OF ACRONYMS AND ABBREVIATIONS

THz	Terahertz
IR	Infrared
Far-IR	Far-Infrared
FPA	Focal Plane Array
FEL	Free Electron Laser
QCL	Quantum Cascade Laser
NEP	Noise Equivalent Power
FE	Finite Element
FTIR	Fourier Transform Infrared Spectrometer
SPIE	International Society for Optics and Photonics
EM	Electromagnetic
TM	Transverse Magnetic
TE	Transverse Electric
RF	Radio Frequency
PEC	Perfect Electric Conductor
PMC	Perfect Magnetic Conductor
PML	Perfectly Matched Layer
DC	Direct Current
SSP	Single Side Polished
PECVD	Plasma Enhanced Chemical Vapor Deposition
UV	Ultraviolet
DFT	Discrete Fourier Transform
DTGS	Deuterated Triglycine Sulfate
Mid-IR	Mid-Infrared
rms	root mean square
PSD	position-sensing detector
CCD	charge coupled device
TCR	temperature coefficient of resistance

THIS PAGE INTENTIONALLY LEFT BLANK

ACKNOWLEDGEMENTS

My thesis was made possible through the help and support of many people. This research was made possible through the funding provided by the Office of Naval Research (ONR) and the National Reconnaissance Office (NRO), and in part through the National Security Institute (NSI) scholarship. Additionally, the fabrication was completed at Oak Ridge National Laboratory, which does not charge for the use of its equipment.

Several individuals provided essential technical support during this project. Sam Barone was indispensable for repairing our electronic equipment and helping us with our laboratory setups, from recommending a better filter for our cooling system to finding exotic resistors and capacitors. I am also grateful for all the salvaging tips he gave us: we put that equipment to good use! Our former machinist, George Jaska, used his impressive skills to help us repair equipment and build essential components, such as the vacuum chamber for the sensor. We have also kept Steven Jacobs busy with new projects such as a cleaving station for the bimaterial sensors. The picture of the multiabsorber wafer in Figure 6 was taken by Jay Adeff. Also, I would like to thank Kirk Benson and Milan Vukcevic for their help in troubleshooting some computer issues. Finally, two former master's students directly contributed to the success of this project: Elison Montagner and Raymond Ng.

The NPS administration and staff have always been very supportive of my thesis while they maintain the delicate balance of academic excellence and Navy requirements. I would like to thank Professor Chris Olsen and his staff, especially Karen Anderson, for responding to my inquiry about the school and ensuring that I was actually hired on time. Cyndy Poenie and Manuela Drury helped me figure out many of the forms and procedures involved in purchasing and travel. Stephanie Hairston provided some needed insight to get our papers published.

The superb instruction provided by the faculty of the NPS Physics Department was essential to completing my doctoral studies. Of particular note, I am grateful for the stimulating demonstrations of Andres Larraza, Brett Borden's challenging exams and

homework assignments, Bob Armstead's spontaneous lectures and insightful quizzes, Pete Crooker's well structured, methodical courses, Scott Davis' very complete explanations of difficult concepts, Jim Luscombe's fantastic lectures and notes, Dragoslav Grbovic's real-world sensor projects, and the amazing ability of Gamani Karunasiri to extract and reveal practical physical concepts from any area he lectures on. I hope to incorporate as much of this wisdom as possible in to any future teaching I am tasked with. Additionally, I would like to thank my dissertation committee for their time and effort and the thorough and insightful feedback they provided to me.

Most importantly, I would like to thank the Sensor Research Lab Terahertz project team: Fabio Alves, Dragoslav Grbovic, and my advisor, Gamani Karunasiri. I certainly could not have completed this project without Fabio Alves, who was my partner and close confidant for this research. He fabricated practically everything personally and we worked closely on setting up all the simulations and measurement techniques. His dedication and determination provided me a steady source of motivation and inspiration. I don't think I ever saw Dragoslav Grbovic lose his infectious enthusiasm despite the constant bombardment of bureaucratic issues he has endured. His extensive knowledge and quick mind were of great help. My advisor, Professor Karunasiri, made this project truly wonderful to work on. He was constantly available for technical help and gently pushed me toward my doctorate, while letting me choose my own research and professional direction. His ability to instantly identify practical concepts (and constants!) has consistently impressed me. Professor Karunasiri leads by example and I always get the feeling he finishes his administrative duties as fast as possible so he can join us working down in the lab. Truly, these team members made my thesis at NPS an enjoyable experience.

Lastly, I would like to thank my parents, Thomas Kearney and Joy Meier. Their constant commitment to professional excellence and public service inspired me to pursue this path in the first place. Their hard work and honesty provide an excellent example for me to aspire to. I don't think I ever doubted that I wanted a career involving lifelong learning, and I thank them for their love and support in helping me meet this milestone.

I. INTRODUCTION

A. TERAHERTZ IMAGING

In recent years, there has been a surge of renewed interest in the terahertz (THz), or Far-Infrared (Far-IR), spectral range. The THz band (Figure 1), so named because the frequencies involved are typically between $0.1\text{--}10 \times 10^{12}$ Hz (3 mm–30 μm wavelength), has some interesting real world imaging applications. Terahertz easily penetrates dry, non-polar, low-conductivity materials (such as common packaging materials and clothing), but is readily reflected by metallic objects and strongly absorbed by water. This limits the effective range, especially above 1 THz, to short-range applications. Additionally, THz radiation is non-ionizing and does not penetrate deeply into the skin, making it potentially safer than X-ray imaging technologies and much less likely to damage objects [1].

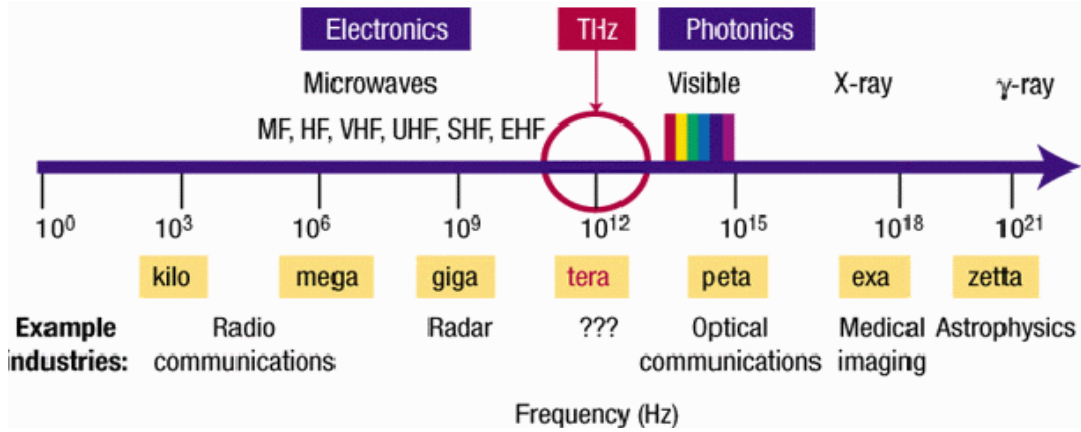


Figure 1. Electromagnetic spectrum showing the location of the terahertz band.
From [2]

Therefore, two of the main interests for THz imaging is security screening [3] and medical imaging [4], [5]. In the case of security screening, metallic objects such as knives are easily observed and explosives are known to have unique absorption spectra in this region allowing them to be identified inside packages without damaging the contents. In the case of medical imaging, much of the interest lies in the absorption of THz by water.

Skin cancers tend to have more blood vessels than surrounding tissue and thus more water content. This can allow one to image cancers with THz [4], [5], perhaps even in real-time during surgery. Cultural heritage conservation [6] is another fascinating application, where THz imaging can be used to identify art obscured by other materials (such as multiple layers of paintings) or help validate the authenticity of priceless objects without damaging them. Additionally, quality control of food [7] can make use of the same principles as medical imaging. Food can be easily imaged inside packages to track how well it has dried, or even in real time to track the efficiency of the process [7]. Unfortunately, detection in the THz range is quite challenging due to the low photon energy necessitating excessive cooling for optical schemes and the high frequency significantly reducing the effectiveness of electronic schemes; these issues create the well-known “Terahertz gap” [8]. Sensors are available in this area, but are prohibitively expensive and bulky, largely restricting them to the research or remote sensing domains.

B. TERAHERTZ IMAGING USING UNCOOLED THERMAL DETECTORS

Uncooled thermal detectors are a well-established, compact and inexpensive technology for imaging in the infrared, especially in the form of microbolometer focal plane arrays (FPAs). Indeed, these sensors naturally evolved in snakes in the form of pit organs leading to a high sensitivity, albeit low resolution, infrared imaging system for 8–12 μm radiation and to a lesser extent the 3–5 μm range [9]. As this sensor is forced to operate at the temperature of the snake (which is the same as the thermal background since they are cold-blooded), it is not surprising that a similar uncooled sensor would perform well when engineered by humans facing similar limitations.

All thermal sensors, including those in snakes, work through a thermally isolated sensitive area heating up when their thermodynamic equilibrium is disrupted by a change in incident electromagnetic radiation. Thermal sensors differ in the way they measure this temperature change; microbolometers, one of the more dominant imaging technologies for uncooled 8–12 μm imaging, work using a layer of material in the thermally isolated region (microbridge) that experiences changes in electrical resistance with temperature. While all materials change resistance in response to a temperature shift, for certain

materials such as titanium (Ti) and Vanadium Oxides (VaO_x), the magnitude of this resistance change is much greater making them especially good choices [10].

As demonstrated in Figure 2, there is a large amount of power in the 8–12 μm infrared range at common temperatures, but power in the THz region is comparatively low. Therefore, active sources are commonly used as illuminators [3]–[7], [11]–[13] for THz imaging systems. Possible active sources include free electron lasers (FELs) [14], quantum cascade lasers (QCLs) [15]–[17], diode based oscillators [18], and nano-electrodes in a photoconductive photomixer [19]. QCLs, in particular, are both compact and powerful, providing a useful narrowband source for imaging. One drawback is that QCLs operate at cryogenic temperatures.

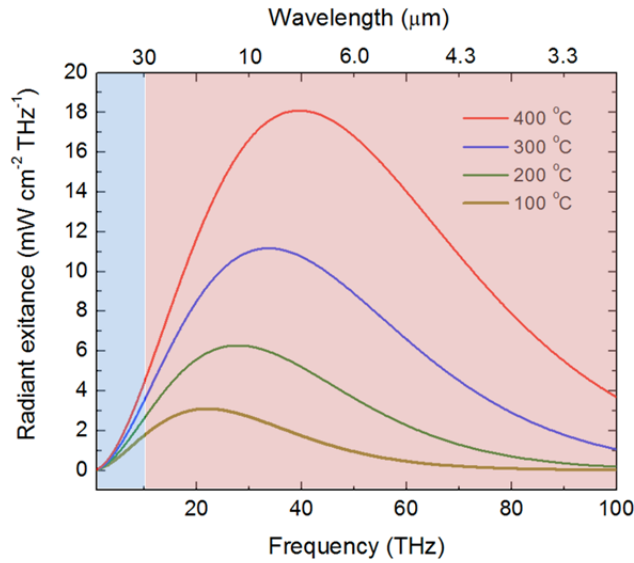


Figure 2. Blackbody distributions for various temperatures with the THz band shaded in blue and IR in red. THz makes up only a small fraction of blackbody emission at common temperatures. From [20].

THz images have been successfully produced using a microbolometer camera and QCL source in a laboratory setting [11]–[13], allowing one to image concealed objects, as shown in Figure 3(a). However, the sensitivity of these microbolometer cameras is limited because the silicon nitride (SiN_x) microbridge is not optimized for high THz absorption [21], [22] as illustrated by the absorption curve in Figure 3(b). Indeed,

uncooled IR microbolometers generally have a noise equivalent power (NEP) in the THz range of approximately $300 \text{ pW/Hz}^{1/2}$ [21] compared to an NEP of $14 \text{ pW/Hz}^{1/2}$ for the IR range [10] implying low responsivity at THz frequencies. Therefore, improving the absorptivity of these microbolometer pixels should improve their performance considerably. Metamaterials, with their subwavelength features, can possess absorption characteristics not found in their constituent materials, which allows fabrication of structures with optimized absorption at THz frequencies. These structures can be incorporated in thermal sensors for enhancing the sensitivity at THz frequencies.

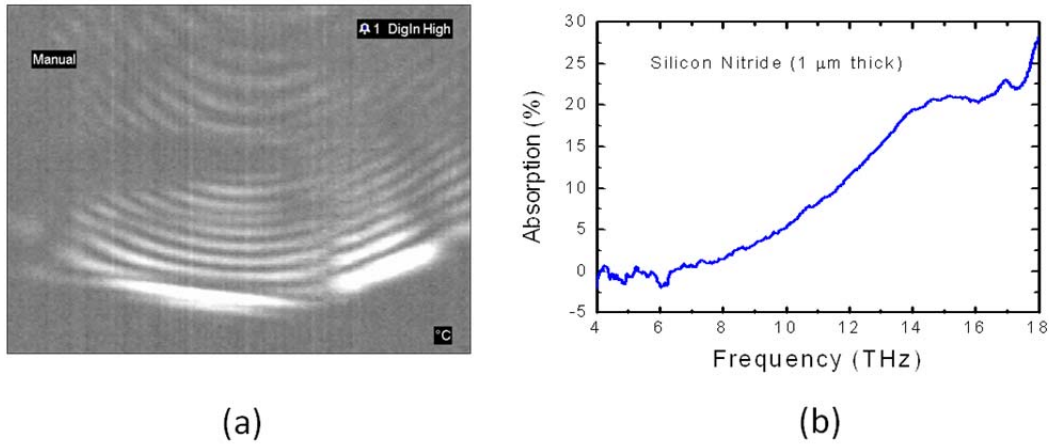


Figure 3. Knife covered in opaque white plastic tape (a) is visible in THz. Absorption (b) of a $1 \mu\text{m}$ thick Silicon Nitride membrane, showing poor absorption in THz. (b) From [20].

C. OVERVIEW OF PRESENT RESEARCH

In the following chapters, I present the research progression from designing, fabricating, and measuring metamaterial absorbers alone, integrated into bi-material sensors, and with a bolometric layer added [23]–[26]. Although each chapter is largely based off a single published work, some of the material has been reorganized for a more logical presentation. Each phase of the research required Finite Element (FE) modeling, clean room fabrication (performed by my colleague Dr. Fabio Alves), and finally measurements in the laboratory using a Quantum Cascade Laser (QCL) source and a

Fourier Transform Infrared Spectrometer (FTIR). The results of this research demonstrate that metamaterials are a promising choice for improving the THz absorption of thermal sensors without compromising their real-time imaging performance. They also offer guidance on how to properly integrate them into microbolometer pixels, allowing one to construct highly sensitive THz microbolometer focal plane arrays in the future.

In Chapter II, metamaterials constructed from fabrication-friendly materials are investigated and optimized. FE analysis is used to guide the fabrication of metamaterial absorbers optimized to absorb nearly 100% of incoming THz power at a specific resonant frequency. The metamaterials are constructed from Al and Si-rich SiO_x ; both of these materials are very suitable for construction of sensors, especially bi-material sensors as elaborated on in Chapter III. The specular reflection of THz radiation by these metamaterials is measured using our FTIR and used to determine the THz absorption of these layers (transmission and higher order scattering are negligible). These results provide us with the information needed to tune metamaterial absorbing layers to the desired frequency with nearly 100% absorption. Finally, the emission properties are also investigated showing that these materials obey Kirchoff's law. The majority of the content of this chapter was published in largely the same form in *Optical Engineering* [23], and presented at the international society for optics and photonics (SPIE) Defense and Security Screening conference in April 2012. The emission section was published in essentially the same form in *Optics Express* [24], and presented at the SPIE Photonics West conference in February 2013.

Chapter III uses the knowledge gained in Chapter II to design and integrate metamaterial absorbers into bi-material pixels. First, the basic physical limitations of thermal sensors are explored and the need for layers with a small thermal capacitance is established. This section is extended from a paper published in *Optical Materials Express* [25]. After this, the details behind design, fabrication, and measurement of bi-material pixels integrated with THz metamaterial absorbers is explored. FE modeling is used to optimize the thermomechanical sensitivity of the pixels, while the data from Chapter II is used to optimize absorption. The sensors are fabricated using standard cleanroom microfabrication techniques and their performance is characterized using a QCL source

combined with an optical readout setup to determine the deflection under THz absorption. This section demonstrates that the metamaterials in Chapter II can be integrated into bi-material pixels, increasing their THz absorptivity. Other than the first section, this work is contained entirely within a paper published in *Optics Express* [26], and was also presented at the SPIE Photonics West conference in February 2013.

Although bi-material pixels face the same thermal challenges that microbolometer pixels do, suggesting that metamaterials will enhance their performance, they do not have the same structure. Indeed, the effect of the bolometric layer in a microbolometer pixel must be explored to ensure that metamaterials can incorporate this layer without having their absorption adversely affected, or the thermal properties of the pixels compromised. Therefore, to investigate this metamaterials with an embedded bolometric layer (in this case, Ti) were fabricated. These metamaterials were fabricated with the bolometric layer at several different depths and the subsequent FTIR measurements demonstrated that if the bolometric layer is close to the ground plane, the absorption is largely unaffected. This information was used to validate the FE model, which also suggests that a bolometric layer with a low sheet resistance will also have a smaller impact on the maximum absorption amplitude. Finally, different possible configurations are explored for their various advantages and disadvantages and future work in the area is suggested. Other than the last sections, this chapter is published practically unaltered in *Optical Materials Express* [25].

The progression from metamaterial absorber design, integration into thermal sensors, and analysis of the impact of a bolometric layer represent significant progress towards the successful integration of THz metamaterial absorbers to enhance the performance of thermal sensors, specifically microbolometers. Chapter II provides the general information necessary when constructing these layers. The results from Chapter III confirm that these metamaterials can be integrated into thermal sensors and that constituent materials that maximize the thermal sensitivity of the sensor can be used while still maintaining high THz absorptivity and a small thickness, highlighting the primary advantage of metamaterials. Finally, Chapter IV confirms that a bolometric layer can be integrated and suggests that this layer should be placed as close as possible to the

ground plane and have as small of a sheet resistance as possible. Ideally, these advances will lead to highly sensitive THz microbolometer cameras using metamaterial absorbers for practical real-time imaging applications.

THIS PAGE INTENTIONALLY LEFT BLANK

II. METAMATERIAL ABSORBERS

Note: *The majority of the content of this chapter was published in largely the same form in Optical Engineering [23], and presented at the international society for optics and photonics (SPIE) Defense and Security Screening Conference in April 2012. The emission section was published in essentially the same form in Optics Express [24], and presented at the SPIE Photonics West Conference in February 2013.*

Metamaterials are artificial structures with subwavelength features that can exhibit overall optical properties not characteristic of their constituent materials. Indeed, they can even have characteristics that are not found in nature, such as a negative refractive index [27]. Absorption in these structures, especially through resistive losses, can be a vexing problem for applications such as superlenses [28]. However, certain applications can benefit greatly from enhanced absorption, such as thermal sensors. Landy et al. [29] initially envisioned a material which would both not transmit light yet would be impedance matched to free space through adjustment of the dielectric and magnetic response of the metamaterial. This would result in a material that could not reflect or transmit light, and therefore must absorb all incident radiation. In practice, this typically is only achievable over certain frequency bands, depending on the geometry of the subwavelength features. Materials with this property have been realized across the electromagnetic spectrum [30]–[43]. In principle, one can fabricate a metamaterial for any frequency within this range of interest by an appropriate adjustment to the geometry of the subwavelength features. Fortunately, this tuning is only weakly dependent on the materials used, so these metamaterial absorbing films can be constructed using standard, mature MEMS microfabrication techniques. These metamaterial films typically consist of a periodic-patterned metal layer, a dielectric spacer, and a ground plane [30]–[43]. In this work, a periodic array of metal squares was used as shown in Figure 4. Metal squares were chosen due to the ease of their fabrication and thin dielectric spacer requirements.

A. SIMULATION

While empirical studies are, of course, essential to evaluate the properties of metamaterials, numerical modeling can very effectively predict the properties of a metamaterial absorber without the need to fabricate every possible geometry. Reflection is suppressed as incident EM waves excite localized surface plasmon resonances, leading to resistive losses in the metal and additional losses in the dielectric layers converting some of the incident energy to heat, allowing the incident radiation to be absorbed [30], [32]. Resonant absorption frequency (ν) and absorption magnitude can be understood using explanations such as impedance-matching to free space [29], an equivalent resistor inductor capacitor (RLC) circuit [30], [32], confined TM cavity modes [44], interference of multiple reflections [45], and transmission lines [46]. However, due to the complex nature of metamaterials, these models are typically guided by finite element (FE) modeling (of at least the patterned metallic layer) [30], [32], [44]–[46]. Therefore, understanding numerical models of metamaterial behavior is essential to predicting their properties. In this work, I used COMSOL Finite Element modeling software. COMSOL is a multiphysics package with many different modules available, but the one used for analyzing metamaterials is the radio frequency (RF) module. Great care must be taken when constructing 3D models, so that one can preserve the physics while still obtaining a result in a reasonable amount of time.

When creating a FE model, boundary conditions and meshing are crucial considerations. The geometry itself is usually fairly straightforward to create and so is of little concern. I should emphasize that the geometry should match the fabricated structure as accurately as possible, as even minor changes in geometry can lead to variations in absorption characteristics. A typical rule of thumb for FE analysis is that elements should be no further than $\lambda/5$ apart, which can result in an excessive amount of mesh if a very large volume of metamaterial is simulated in a 3D model. To simplify the situation, we can exploit the fact that metamaterials are periodic structures and thus any electromagnetic solution must satisfy periodic boundary conditions. Therefore, only a single unit cell of metamaterial (see Figure 4(a)), with appropriate periodic boundary conditions, is necessary for FE analysis. For radiation normally incident to the surface,

the electric and magnetic fields of an incident plane wave can be broken into two polarizations with fields normal to the boundaries. In this case, a perfect electric conductor (PEC) will enforce periodic boundary conditions for electric fields normal to the boundary, while a perfect magnetic conductor (PMC) will do the same for magnetic fields normal to a boundary. In the case of radiation not normally incident to a surface, Floquet boundary conditions are appropriate as they attach the necessary phase factor to the radiation [47]. However, in most thermal sensor applications radiation is near normal incidence making normally incident radiation a good approximation.

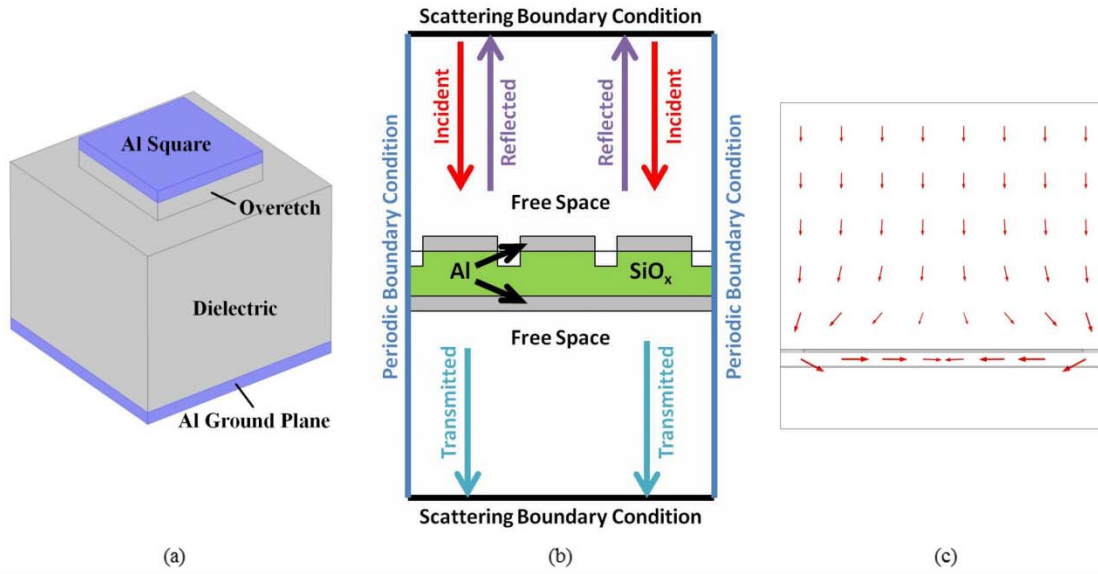


Figure 4. Unit cell (a) of a metamaterial with a single absorption peak. The model also incorporates the unintentional over-etch into the SiO_x during the fabrication. Schematic representation (b) of the unit cell in the FE modeling program with boundary conditions and THz plane wave at normal incidence. Time-averaged power flow (c) near the resonant absorption frequency and arrow lengths relate to magnitude in log scale. From [23]

The model must also allow electromagnetic radiation to interact with the metamaterial absorbers. To accomplish this, one must choose the proper boundary conditions for the surfaces intended to allow radiation to penetrate through. One surface must somehow generate, or allow penetration of, incident radiation and also allow reflected radiation to leave the model or absorb it without allowing any radiation to

reflect back in. The second surface, typically “below” the ground plane, must allow any transmitted radiation to leave the model or absorb it, also without any radiation reflecting back into the model. Several popular methods available in COMSOL are scattering boundary conditions, internal ports, and perfectly matched layers (PMLs). Scattering boundary conditions are meant to approximate an infinite space or “open” boundary for radiation to propagate out into. They work as first order absorbing boundary conditions for plane, cylindrical, or spherical waves. Port boundary conditions are similar in that they are perfectly absorbing boundary conditions for general modes of known shape. Both of these boundaries can also allow the same types of waves to penetrate the boundary *into* the model, supplying the incident radiation. The power is easily controlled by adjusting the Poynting vector and can be calculated using $A(\vec{S} \cdot \hat{n})$ for plane boundaries. While not exactly a boundary condition, a PML can also be used to approximate an open boundary. A PML is actually very similar to the initial idea of a metamaterial absorber; it is impedance matched to the material that it is adjacent to so that it can eliminate reflection and uses a complex coordinate transformation to cause an incident electromagnetic wave to decay as it propagates resulting in essentially total absorption [47]. The PML actually has a finite thickness and must have additional mesh elements, and should usually be coupled with a scattering boundary condition to minimize back reflections. All of these tools tend to work very well for a particular wave mode and propagation vector and then start to allow some reflection back into the model, so care should be taken in their implementation. A schematic of this setup is shown in Figure 4(b).

Once boundary conditions, geometry, and meshing are finished, the wave equations for the model to solve must be specified. The default option for COMSOL is “relative permittivity” which solves the EM wave equation of the form:

$$\nabla \times \mu_r^{-1} (\nabla \times \vec{E}) - k_0^2 \left(\epsilon_r - \frac{j\sigma}{\omega\epsilon_0} \right) \vec{E} = 0 \quad (1)$$

Thus, this equation admits relative permeability and permittivity as well as conductivity. This is convenient for materials that can be defined entirely by permeability

and permittivity, such as free space, or those where conductivity dominates, such as most metals in THz. For some metals, frequency-dependent conductivity is needed if it varies appreciably within the frequency range of interest (such as Au [44]). In the case of Al used in our metamaterial structures, the relaxation is fast enough that the Drude model approximates to the DC conductivity [49]. It should be noted that thin films of metals do not have the same conductivity as bulk metals and also may have variable conductivities depending on deposition technique and surface [49]. COMSOL does have a “Drude-Lorentz dispersion model” option, but this approximation renders it unnecessary for Al as absorption remains largely unchanged. The second convenient setting is “Refractive index” which solves the EM wave equation of the form:

$$\nabla \times (\nabla \times \vec{E}) - k_0^2 \epsilon_r \vec{E} = 0 \quad (2)$$

Clearly, this form assumes relative permeability is 1 and conductivity is contained in the relative permittivity via the extinction coefficient [46]. It then calculates the permittivity using the complex refractive index: $\epsilon_r = (n - ik)^2$, using the usual convention that a positive “ k ” refers to loss while a negative “ k ” is gain. This form is useful for dielectrics, where the permeability can largely be ignored, and the literature commonly specifies the complex refractive index.

Once the model construction is complete, the solvers must be chosen. The models in this work use a frequency domain solver, which simply solves the EM wave equations at specified frequencies. This results in the E and B-field solutions allowing one to determine information such as power flow (see Figure 4(c)). More resolution simply correlates to a longer computation time, but more precise absorption curves. Of greater consequence is the type of solver used. Direct solvers are preferable if the modeling computer possesses sufficient memory as there are no convergence issues, yet indirect solvers can solve denser meshes with the same resources but can have convergence issues. Thus, the choice of solver and settings will largely be determined on a case-by-case basis. Direct solvers were used for the models in this work, due to the computational resources available. In addition, parametric sweeps can be used to run several different configurations of metamaterials together.

Finally, once the model has finished its run, one must extract absorption characteristics. In all cases, when magnetic losses are largely ignorable in the constituent materials, a convenient way to extract absorption is through performing volume integrations of the resistive losses in the metamaterial. Non-linear effects are largely ignored in these models, so the incoming power can be set to 1 W and the absorption can simply be read off as the Watts of power absorbed in the metamaterial. This also has the advantage of identifying which layers are actually heating up, allowing one to more effectively model metamaterials that are not thermally linked as in Figure 5.

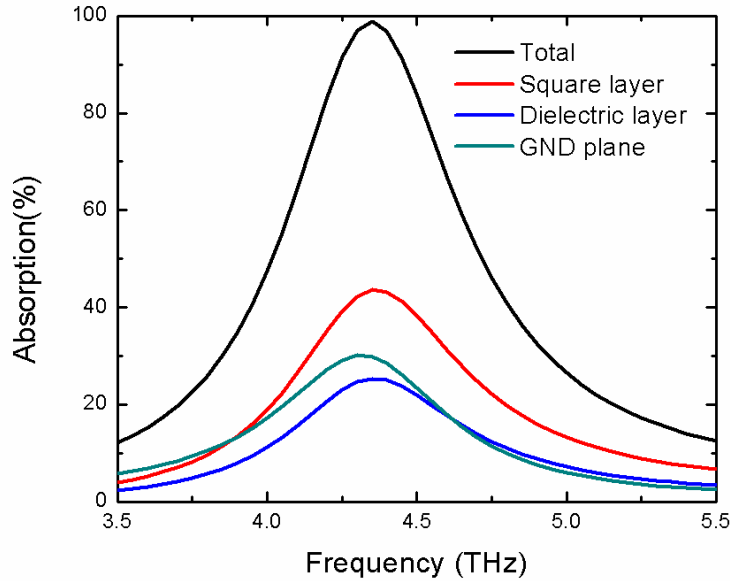


Figure 5. Modeled absorption characteristics of the three layers of a metamaterial with single absorption peak. From [23]

Additionally, when using ports, one can also extract transmission and reflection coefficients by inverting the S parameters. This method is also important for the reflection model that relies on the resonator layer having some frequency dependent reflection coefficient [45]. This, of course, assumes that higher order scattering is largely ignorable which should be true for sub-wavelength features of this kind and is known to be small for metamaterials in other frequency ranges [46]. In practice, transmission

through a metamaterial is vanishingly small due to the optically thick ground plane of approximately 100 nm. The skin depth of Al layers is approximately 80 nm for 1 THz, and both models and measurements show no significant transmission. Finally, reflection and transmission coefficient techniques and resistive loss can be used together to validate that models are working correctly [30].

B. FABRICATION

Metamaterial absorbers, whether split ring resonators or arrays of squares, typically consist of a patterned metal layer, a dielectric spacer of some kind, and a ground plane. Variations including a bolometric layer and integration into bi-material sensors will be discussed in later chapters. Fabrication of these layers is easily done using standard microfabrication techniques. This was performed at Oak Ridge National Laboratory by Doctor Fabio Alves and Assistant Professor Dragoslav Grbovic. At every point in the fabrication, the materials were carefully monitored for relevant parameters such as residual stress and DC conductivity. These measurements were performed with stylus profilometry and optical interferometry in the case of thickness, four-point probe measurements in the case of conductivity, and wafer curvature measurements using a stylus or optical profilometer to evaluate residual stress. As transmission is essentially zero due to the thick ground plane of the metamaterial [30], [48], one does not need to use low conductivity substrates as with thin metal films [49]. If conductivity of the wafer is a concern, a layer of insulating dielectric can be deposited. Therefore, a single side polished (SSP) Si wafer of any thickness or doping concentration should be suitable, but thicker wafers are less fragile. Generally 500 μm thick wafers were used due to the low price and durability of these wafers.

The first step is to deposit the metallic ground plane. We typically used Al deposited using an e-beam evaporator due to the fast deposition rate, good adhesion, and good conductivity. Typically, these Al layers were measured to have a DC conductivity of 10^7 Siemens/meter for layers of approximately 100 nm. The bulk conductivity of Al is over 3 times larger than that of the Al films, therefore measurement with a four-point probe is essential. The second step is the dielectric spacer, which in this work was SiO_x .

Specifically, this was a low stress oxide deposited with a Plasma Enhanced Chemical Vapor Deposition (PECVD) system at 350°C with more Si than the standard SiO₂ formulation (-13 MPa compared to -140 MPa). Dielectric film parameters can vary between machines and even through small changes in machine parameters; therefore, great care was taken to reproduce the same SiO_x for every phase of the project. Finally, a second Al layer is deposited on top of this dielectric. The layer is deposited using exactly the same settings as the ground plane metal. To pattern this layer and form a metamaterial, it must be etched. First, after the wafer is prepared, photoresist is spun on using a spin coater. After some baking steps specific to the photoresist, the wafer is placed into a contact aligner. A mask with the metamaterial absorber resonators is then placed on top of the wafer and the photoresist is exposed to UV light. After this, the photoresist is developed and processed further, again with steps specific to the type of photoresist. In this work, positive photoresist was used, so unexposed areas remained on the wafer while exposed areas were dissolved. To remove the unwanted, now exposed Al, an Ar plasma sputter etcher was used. The sputter etcher accelerates Ar ions at the wafer, removing both photoresist and exposed Al. This etcher is anisotropic (directional) which reduces the “undercut” one would get from isotropic etching techniques such as acid etching. The remaining photoresist protects the Al that we wish to stay on the wafer. Unfortunately, this process is not very selective between Al and the underlying dielectric and the etching must occur long enough to go all the way through the Al layer. This results in an effect known as “over-etch” where some of the dielectric is also removed as illustrated in Figure 4(a). The effect of over-etch can be accounted for in simulations by simply adding to the geometry. Finally, the photoresist is removed using appropriate chemicals and an isotropic oxygen plasma “barrel” etcher. The result is a wafer with 25 different metamaterials pictured in Figure 6.

It should be noted that other materials and processes can be used. Indeed, acid etching (aka “wet” etching) is much more selective and could result in no over-etch into the dielectric. If the etching is carefully controlled and reproducible, it may well be a better choice than sputter etching. Other suitable choices for the Al etching include reactive ion etching and liftoff. The advantage of reactive ion etching is its better

selectivity towards Al. In the case of liftoff, the photoresist is deposited *first*. Inverted masks are used such that the unwanted Al is deposited on the photoresist and is removed with it. This requires no metal etchant at all, and is therefore faster and easier, albeit with less precision. Also, other materials can be used for metals include Au or Ag or dielectrics such as SiN_x and polyimides.

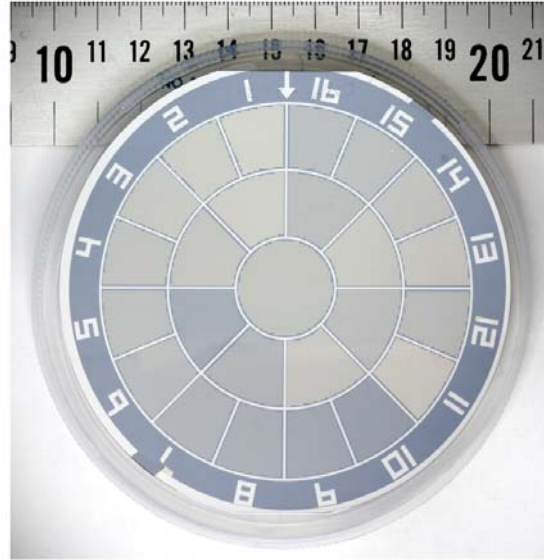


Figure 6. One of the fabricated wafers with 25 different metamaterials arranged radially for automated reflection measurements using a PIKE MappIR FTIR accessory. From [23]

C. MEASUREMENT

To evaluate the THz optical properties of the metamaterial structures, a Fourier Transform Infrared Spectrometer (FTIR) was used. This device consists of a Michelson interferometer with a moving mirror in one arm; this results in periodic oscillations in amplitude whose frequency depends on the wavelength of radiation and velocity of the mirror. Thus, the FTIR's thermal detector can measure every frequency simultaneously and extract the frequency data with a Discrete Fourier Transform (DFT). This powerful technique is applicable across the frequency spectrum, but is particularly effective for the Infrared region of the spectrum. The FTIR available at NPS is a Thermo-Nicolet Nexus 870 fitted with a globar source (hot SiC filament) and a Deuterated Triglycine Sulfate

(DTGS) pyroelectric detector with a polyethelene window. This is the recommended configuration for Far-IR spectrometry (defined by Nicolet as 50–600 cm^{-1} or 1.5–30 THz); however, the 1.5–3 THz range is difficult to use due to the fact that the source power is relatively low as shown in Figure 7. For measurements in the Mid Infrared (Mid-IR) range (defined by Nicolet as 7400–350 cm^{-1} or 1.35–28.6 μm), the beam splitter is changed to KBr and the detector is changed to a Thermoelectrically cooled DTGS detector with a KBr window. For metamaterial absorption, the Far-IR configuration is of important as it contains the THz range of interest. In terms of FTIR settings and configurations, one must achieve a large enough signal to align the FTIR, yet a small enough signal to avoid saturation of the detector. In the default configuration of the FTIR, it can only measure transmission through a sample.

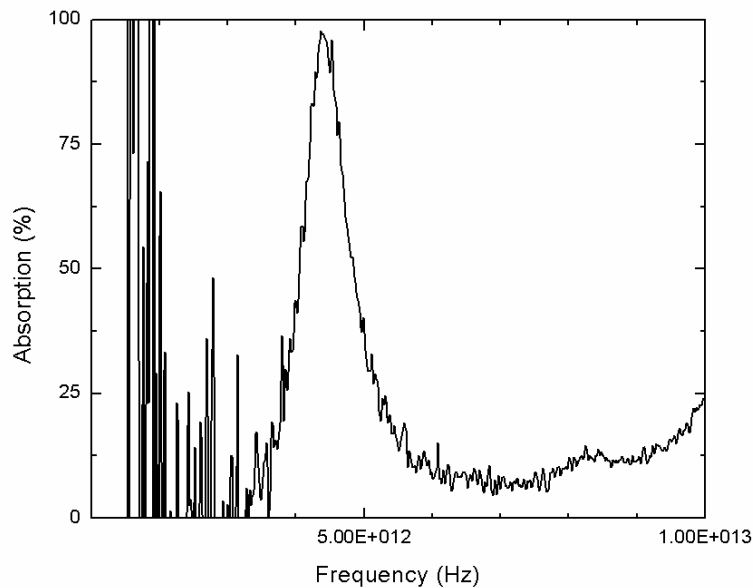


Figure 7. Raw FTIR data for a metamaterial absorber, showing the excessive noise in the spectral region below 3 THz.

Clever use of optics can allow one to measure reflection as shown in Figure 8; specifically, an FTIR accessory known as MappIR can be programmed to automatically measure either transmission or reflection at predefined points on a wafer resulting in a

significant time savings when dealing with a large number of metamaterials. In the case of emission measurements, the FTIR is programmed to see the metamaterials and a black carbon blackbody (prepared by depositing candle soot on a suitable substrate) as an external source. An off axis parabolic mirror collimates the thermal radiation from a small area of the sample on a hot plate and directs it into the FTIR. In all of these configurations, the THz must pass through the outside air, leading to frequency dependent losses that cannot be ignored. The inner area of the FTIR is purged with clean, dry, low CO₂ air to preserve the optics and boost signal strength. Despite this a background spectrum must *always* be taken in FTIR measurements to subtract the non-uniform spectral characteristics of the system. Appropriate backgrounds depend on the measurement and configuration, but typically are air for transmission, thick uniform Au or Al films for reflection, or black carbon blackbodies for emission. The FTIR can automatically compare these measurements to the sample or they can be done in the graphing software. Typically the output is given in “percent transmission” which essentially divides the sample points by the background points. This results in sizable errors when the signal is much smaller than the noise as seen for the 1.5–3 THz range in Figure 7.

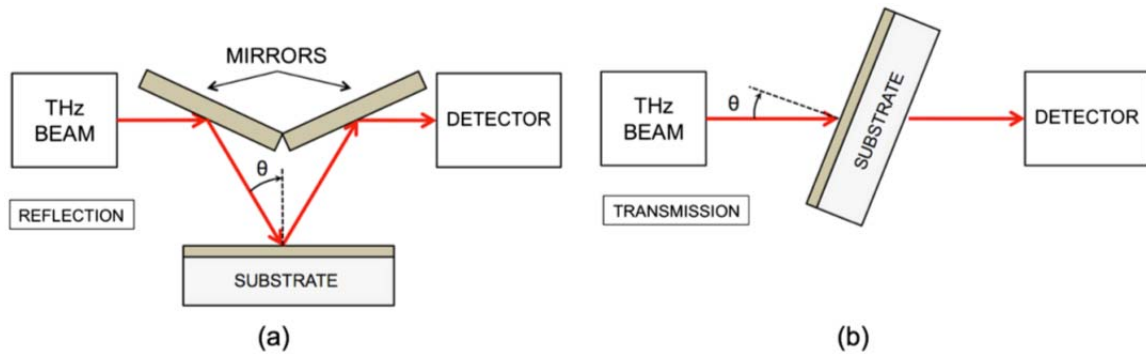


Figure 8. Schematic representation of the experimental configuration used for measuring the reflection (a) and transmission (b), before using the MappIR accessory. The accessory performs essentially the same measurements, but operates at an incident angle of 15 degrees. From [49].

D. OPTIMIZATION AND TUNING OF SINGLE-BAND METAMATERIAL ABSORBERS

The simplest metamaterial geometry contains only one type of square arranged in a periodic array. I refer to them as “single-band” absorbers because they have only one absorption peak in the frequency range of interest. As Figure 9 demonstrates, we see that the lowest order confined mode consists of a single oscillating dipole formed by the incident radiation interacting with the square with opposing currents and charges in the ground plane.

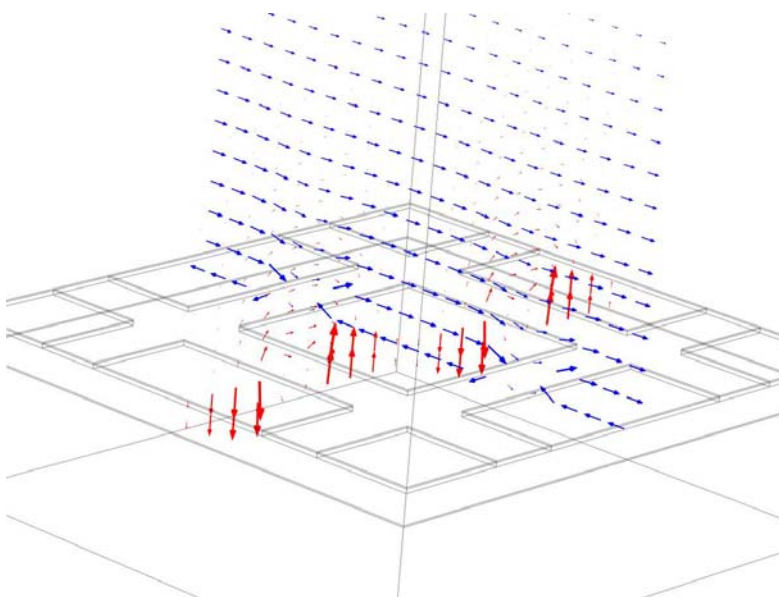


Figure 9. FE model solution for $16\ \mu\text{m}$ squares at the resonant absorption frequency. Electric (red) and magnetic (blue) fields for a metamaterial absorber at its resonant frequency. Note the opposing electric fields on either side of the square and the reversal of the magnetic field.

This suggests that we should expect the wavelength of any trapped first-order modes should be proportional to the size of the structure in the direction of the incident E-field component parallel to the surface. Of course, this does not take into account the boundary conditions or the coupling between squares. Figure 10(a) shows experimental results for single band absorbers with the same $21\ \mu\text{m}$ periodicity, but incrementally increasing square size. As expected, the resonant frequency decreases as square size increases. Figure 10(b) shows that the resonant frequency is roughly proportional to the

inverse of the square size, as expected due the fact that wavelength is inversely proportional to frequency. Therefore, modifying square size is an effective method for controlling the resonant absorption frequency.

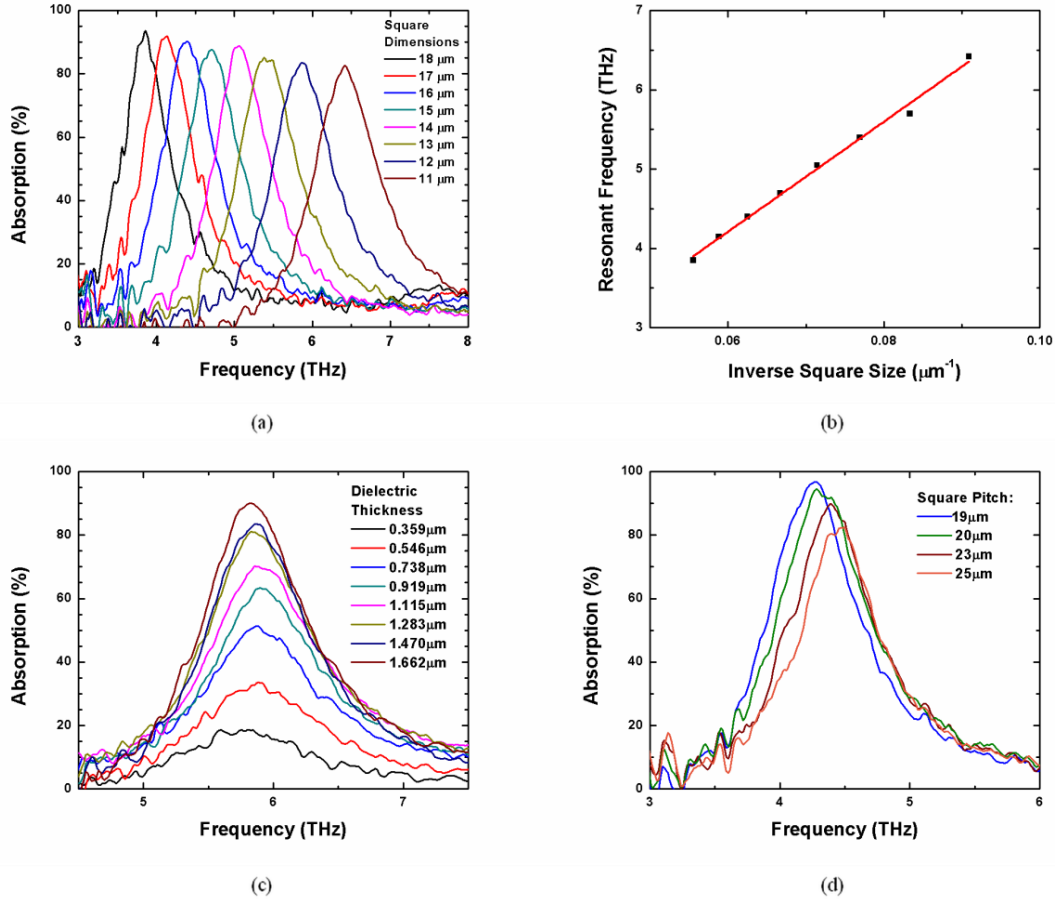


Figure 10. FTIR measurements (a) for varying square size, 21 μm pitch, and 1.47 μm SiO_x . Linear fit (b) of inverse square size ($1/s$) to resonant absorption frequency (ν). The effects of varying dielectric thickness (c) for 12 μm squares and 21 μm pitch and varying pitch (d) with 16 μm squares and 1.47 μm SiO_x . From [23]

Now that the most effective frequency tuning method has been established, we must optimize the remaining geometric parameters to achieve the highest possible maximum absorption amplitude. Dielectric thickness and periodicity are known to be significant parameters for maximum absorption. As Figure 10(c) demonstrates, a higher dielectric thicknesses typically result in higher absorption. As no reduction in absorption amplitude

was observed for increased thickness in this range, it seems that all absorbers have an optimal thickness at or above $1.66\text{ }\mu\text{m}$. Once past this optimal thickness, absorption magnitude will decrease with increasing thickness until another optimal thickness is approached. The reflection model of absorption suggests that, similar to thin film interference, there should be several optimal thicknesses. In the case of thermal sensor applications, we will see that in most cases these materials should be as thin as possible. Periodicity, or pitch, shows a similar relationship to dielectric thickness, showing more significant frequency shifts as demonstrated in Figure 10(d). Intuitively, a smaller pitch should correspond to a higher absorption due to a higher density of squares [30], [32] or better coupling to external radiation [44]. It should be noted that there is a relationship between pitch and dielectric thickness such that a given dielectric thickness will have an optimal pitch. As Figure 11 shows, simulations suggest that at certain thicknesses increasing pitch can increase absorption magnitude. While this is certainly relevant if one wishes to construct very thick absorbers, in the thin regime a decrease in pitch will always be desirable. Of course, any resonant absorption frequency shifts due to periodicity or dielectric thickness changes must be compensated for through tuning the square size.

While metamaterial absorbers can be constructed using many different materials, the materials used do have a significant impact on the optimal dimensions for the metamaterial geometry. Metals, or equivalent high conductivity materials, must have sufficient thickness and conductivity to function as resonators. Additionally, some metals such as Au have conductivities that vary greatly across 1- 10 THz [44], [45], [48]. However, the Al films used in this experiment have essentially the same conductivity across the 3–8 THz range [48]. The refractive index of the dielectric spacer is also significant, as it will relate to the capacitance of the squares or the wavelength of the trapped dipole modes, resulting in higher absorption frequencies for lower refractive indexes. Additionally, processing steps that over-etch into the dielectric cannot be ignored. This removes dielectric from around the squares, causing a shift in resonant absorption frequency. This could, of course, be used intentionally to shift resonant frequency and reduce the thermal mass of the absorbers if desired.

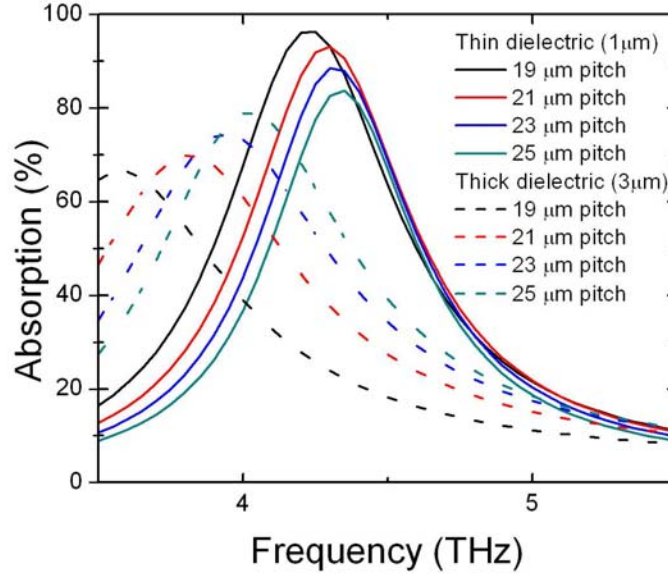


Figure 11. Simulations for 16 μm square size and 21 μm pitch with two dielectric thicknesses showing that for thicker cases, increasing periodicity can, in fact, increase percent absorption.

E. OTHER METAMATERIAL CONFIGURATIONS AND EMISSION CHARACTERISTICS

While single band metamaterial absorbers are ideal for coupling with a single narrowband source such as a QCL for active THZ imaging, in some cases a broader absorption peak may be desired. Additionally one might require two absorption peaks, for instance when working with two separate QCL sources. Metamaterials can be fabricated with these properties by using more complex unit cells. A possible configuration is to simply alternate the squares resulting in a pattern reminiscent of a checkerboard, as illustrated in Figure 12(a) with squares dimensions of 13 and 17 μm and a dielectric layer thickness of 1.47 μm . Figure 12 shows the measured (b) and simulated (c) absorption of structure in (a) along with absorption spectra by removing one type of squares and keeping the rest of the parameters the same.

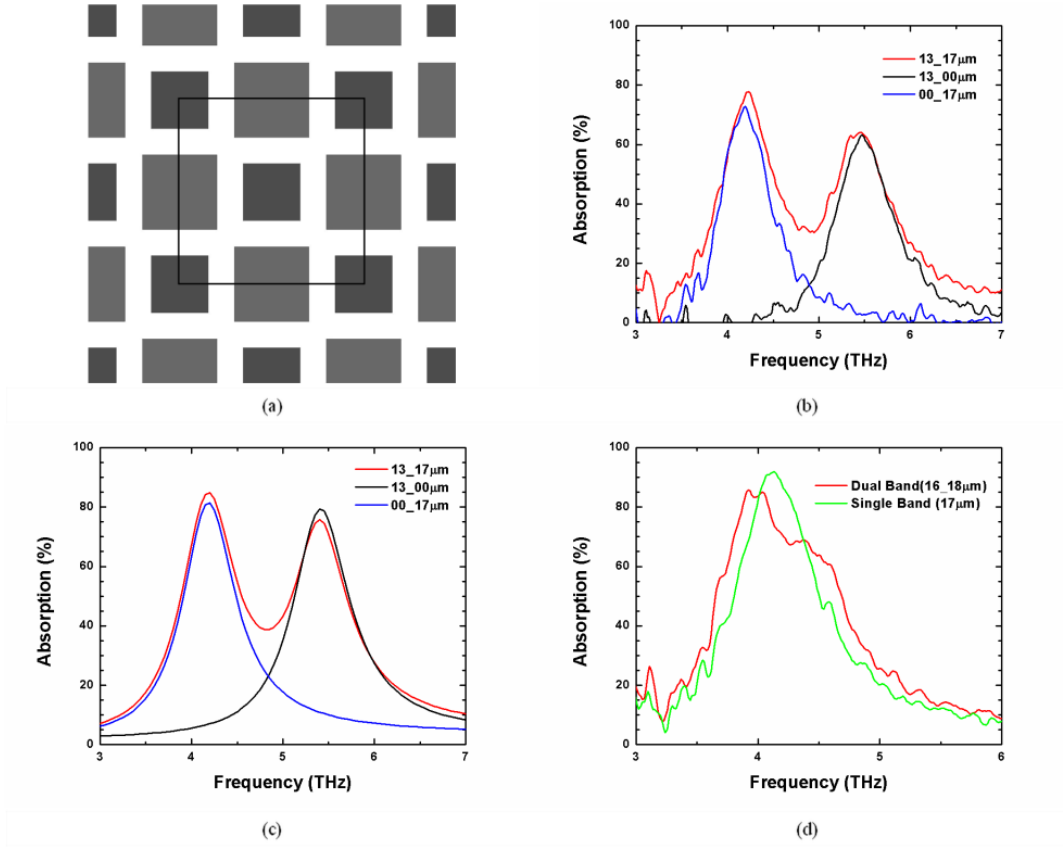


Figure 12. Unit cell (a) of a dual band metamaterial configuration. Measured (b) and modeled (c) absorption for a dual-band absorber with squares that have a 4 μm size difference compared to the same configuration with only one type of square. Comparison (d) of the absorption spectrum for dual band absorber with 2 μm square size difference, overall pitch of 42 μm and SiO_x thickness 1.47 μm to a single band absorber with an intermediate square size. From [23].

It can be easily seen from Figure 12(b) that each type of square is responsible for one of the two peaks of the combined structure absorption. For the configuration shown in Figure 12(a), the absorption measurement shows two well-separated absorption peaks at 4.25 and 5.5 THz similar to that obtained in the simulation. In addition, Figure 12(b) shows measured single-band absorption from two complementary structures fabricated with only one type of square while maintaining the same dimension and pitch. In this case, single-absorption peaks clearly match with the absorption peaks of the dual-band absorber, indicating that each set of squares in Figure 12(a) is responsible for generating the two peaks as predicted by the FE model (Figure 12(c)). As the difference in

dimensions of square size is reduced (16 and 18 μm), the absorption peaks begin to overlap and merge together as illustrated by measured data in Figure 12(d). Thus, by bringing the size of the squares closer together, it is possible to produce a broader absorption peak than a single square configuration of intermediate size (17 μm). In both the measurements and the FE model (Figure 12 (b) and (c), respectively), it is apparent that the lower frequency absorption is enhanced while the higher frequency peak is suppressed. This causes the asymmetric peak shown in Figure 12(d), as the two absorption peaks are merged by making the dimension of squares close to each other. This can partially be explained by the fact that the smaller squares are more active at the larger square resonant frequency than vice versa as shown in Figure 13.

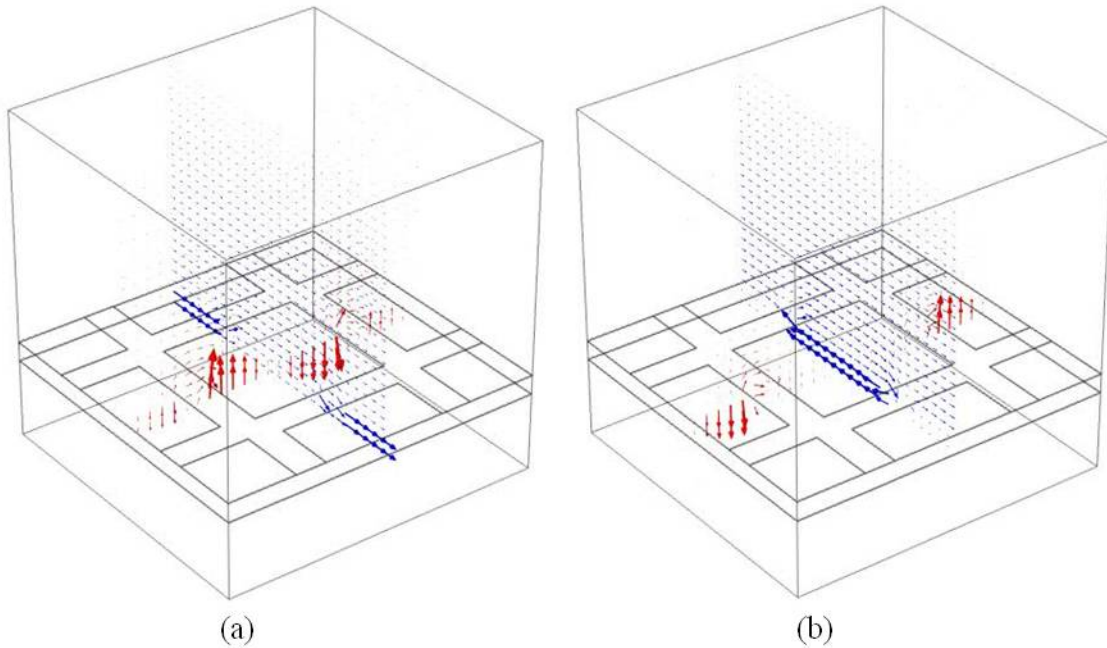


Figure 13. FE model solution for 16 and 18 μm squares at the resonant absorption frequency of the 18 μm squares (a) and the 16 μm squares (b). The center square is 18 μm . Electric (red) and magnetic (blue) fields are shown. Note how the 16 μm squares have a larger electric field in (a) than the 18 μm squares do in (b) showing that the 16 μm squares assist the 18 μm at their resonance, but not vice versa.

Another configuration for producing two absorption peaks is shown in Figure 14(a) where smaller squares are placed around larger ones in a tile-like pattern. This

configuration allows for squares with large size differences, and therefore absorption peaks at widely separated frequencies, to be more densely packed to increase absorption magnitude as demonstrated in Figure 14(b). Measurements showed two distinct absorption peaks at frequencies 4 and 6.5 THz, as depicted in Figure 14(b), with the high frequency peak associated with the smaller squares, as expected. Additionally, the higher frequency peak has a consistently larger magnitude, most likely due to the higher density of $10\ \mu\text{m}$ squares. It is also apparent that the strength of the peak at 6.5 THz drops faster compared to the one at 4 THz as the thickness of the dielectric layer is increased. The 6.5 THz peak seems to be much more sensitive to changes in dielectric thickness compared to single-absorption peak configurations, such as in Figure 10(c).

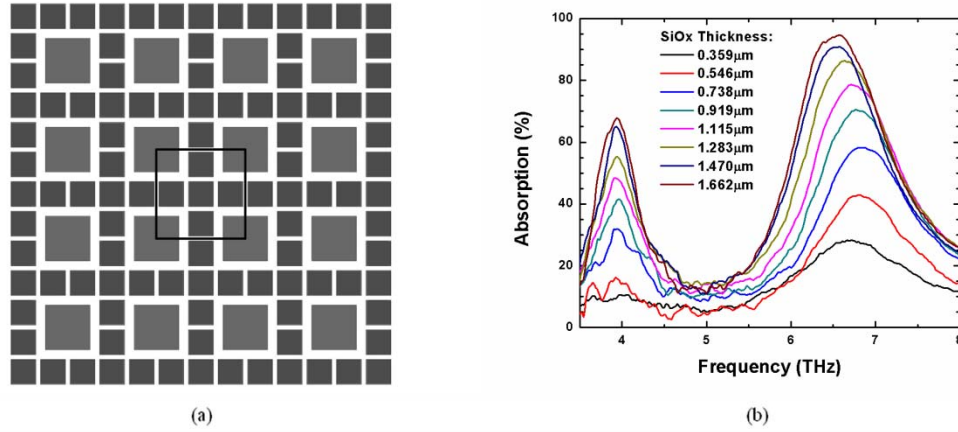


Figure 14. Unit cell (a) and absorption characteristics (b) of a two peak metamaterial layer utilizing a tile configuration to maximize square density. From [23].

The number of absorption peaks can be extended from dual-band absorbers by introducing additional square sizes. The geometry in Fig. 15 (a) has three different squares (11, 14, and 17 μm) and maintains symmetry in two directions, thus remaining polarization-independent at normal incidence, while also allowing for one of the squares (in this case the 14 μm squares) to have a 20% higher density, enhancing absorption at one of the corresponding resonant frequencies. This enhancement can be useful to increase absorption selectively if desired. As with the dual-band configuration, three distinct peaks associated with each square size can be resolved in the measured absorption spectrum in Fig. 15(b). In this case, the middle peak at 5 THz has a higher

square density associated with it and an absorption peak of similar magnitude compared to the one corresponding to the larger squares at 4 THz. The overall absorption was found to be lower than that obtained for single-band and dual-band metamaterials, likely due to the lower density of particular square sizes in this configuration.

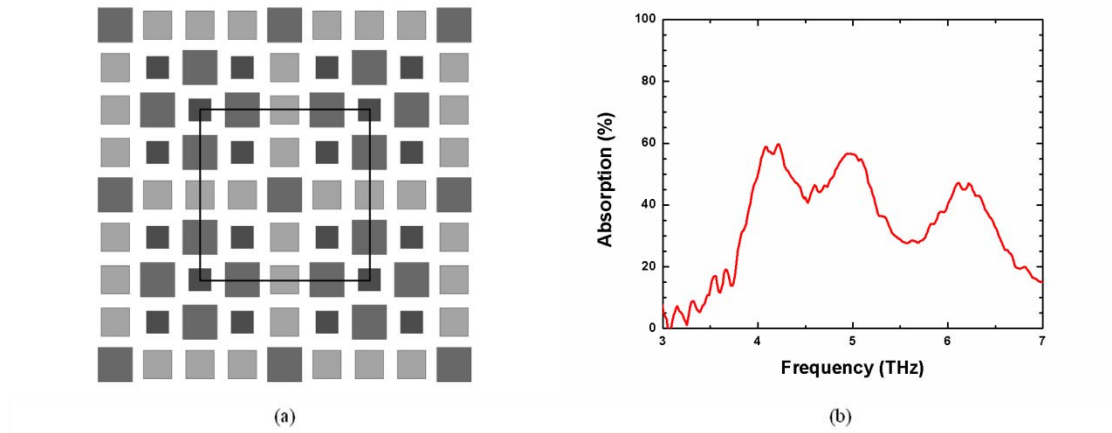


Figure 15. Unit cell (a) and measured absorption (b) for a triple band metamaterial configuration with square sizes of 11, 14, and 17 μm showing three clear peaks. From [23].

As metamaterial absorbers have a narrowband absorption peak, Kirchoff's Law demands that they also possess a narrowband thermal emission peak [50], [52]. Indeed, the emissivity of the metamaterials should follow their absorptivity exactly for thermal equilibrium to be upheld. As described earlier, this was tested using the metamaterial absorbers as an external source for the FTIR and comparing it to a blackbody. Samples A, B, and C consisted of single band absorbers with 17 μm , 13 μm , and 9 μm squares, respectively. All samples had 21 μm periodicity and 1.6 μm thick dielectric spacer of stoichiometric SiO_2 . The emission spectrum of a reference emitter (a silicon wafer coated with black carbon) was used to extract the emissivity of the metamaterial samples as a function of THz frequency. The emissivity spectra, shown in Figure 16 were obtained by dividing the sample data by the corresponding data obtained using the blackened emitter heated to the same temperature (400 $^{\circ}\text{C}$).

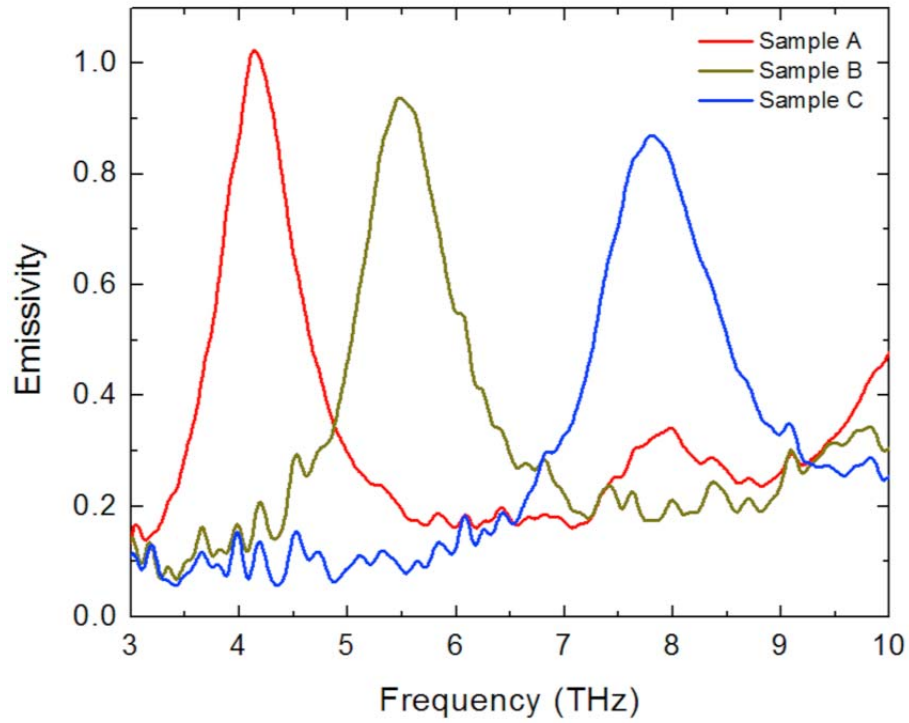


Figure 16. Measured emissivity of the metamaterial samples A, B and C at 400 °C. Emissivity exhibits peaks at 4.1, 5.4 and 7.8 THz, respectively. From [24].

It is clear that the emission spectra in Figure 16 agree well with the measured absorption data in Figure 16 as expected from Kirchhoff's law. The emission bandwidth at half maximum for each metamaterial structure is approximately 1 THz.

The total power emitted into each THz band per unit area (P) can be estimated by integrating Planck's blackbody radiation formula ($P(\nu)$) multiplied by the measured emissivity ($\epsilon(\nu)$) within the emission bandwidth as:

$$P(\nu) = \frac{2h}{c^2} \int \frac{\epsilon(\nu) \nu^3}{\exp\left[\frac{h\nu}{kT}\right] - 1} d\nu \quad (3)$$

where h is Planck's constant, c is the speed of light in vacuum and k is Boltzmann's constant. The estimated power per unit area, based on Eq. (3), for samples A, B and C operated at 400°C is 11, 18 and 36 W/m², respectively.

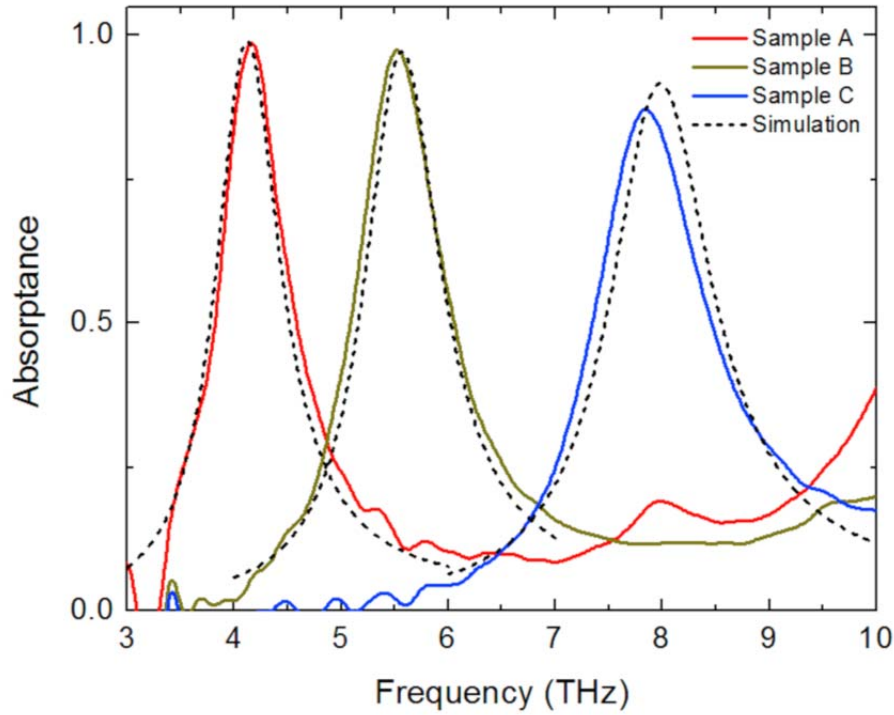


Figure 17. Spectral absorbance of the metamaterial samples A, B and C. Solid lines represent the measured absorbance with peaks at 4.1, 5.4 and 7.8 THz, respectively. Dashed lines represent the finite element simulation results. From [24].

THIS PAGE INTENTIONALLY LEFT BLANK

III. METAMATERIALS INTEGRATED INTO THERMAL SENSORS

Note: *The first section is extended from a paper published in Optical Materials Express [25]. The remaining material in this chapter is contained entirely within a paper published in Optics Express [26], and was also presented at the SPIE Photonics West conference in February 2013.*

A. THERMAL SENSOR PROPERTIES

To achieve an increase in performance for thermal sensors, we must first consider their performance characteristics. The two most significant parameters are the thermal time constant (τ) and responsivity (R_{th}). All thermal sensors have a thermally isolated sensitive region which disperses heat to the environment through radiation, convection and conduction as illustrated in Figure 18.

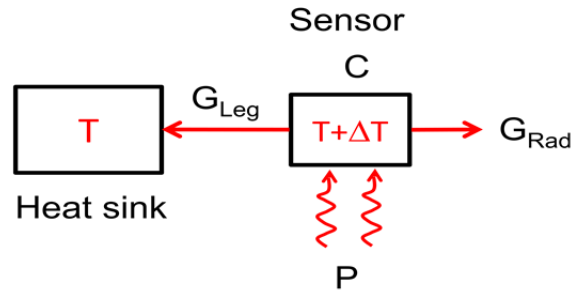


Figure 18. Diagram showing heat exchange between a thermal sensor and its environment. Incoming power P creates a gradient of ΔT between the sensor and the heat sink at temperature T in addition to radiation losses. Convection losses are ignored as most sensors operate at low pressures. After [20].

Radiation losses are unavoidable and intrinsic to all thermal sensors as Kirchoff's law [50] demands that any object that absorbs radiation must possess the same emissivity, and it is clear that THz metamaterial absorbers are no exception [24]. Convection can be controlled through the gas pressure of the surrounding environment [52] and conduction through materials and structural design of the sensors. If the thermal losses can be approximated as linear with respect to the temperature gradient (ΔT) between the

thermally isolated sensitive area and the surrounding environment, they can be lumped into a single constant term called the thermal conductance (G_{th}). Therefore, the heat exchange equation for a thermal sensor absorbing radiation of power (P_{th}) will be:

$$P_{th}(t) = G_{th}\Delta T + C_{th} \frac{d\Delta T}{dt} \quad (4)$$

where C_{th} is the thermal capacitance of the thermally isolated sensitive area. Solving this differential equation, we can then arrive at a formula for the responsivity of a detector under sinusoidal illumination power [10]:

$$R_{th} = \frac{\Delta T}{P_0} = \frac{\eta}{G_{th}\sqrt{1+\omega^2\tau^2}} \quad (5)$$

where η is the absorbance, the fraction of incident power (P_0) absorbed by the sensitive region of the detector, τ is the thermal time constant ($\tau = C_{th}/G_{th}$) and ω is the angular modulation frequency of the incident radiation. The graph of R_{th} vs G_{th} in Figure 19 shows that reducing thermal conductance is always advantageous in terms of responsivity.

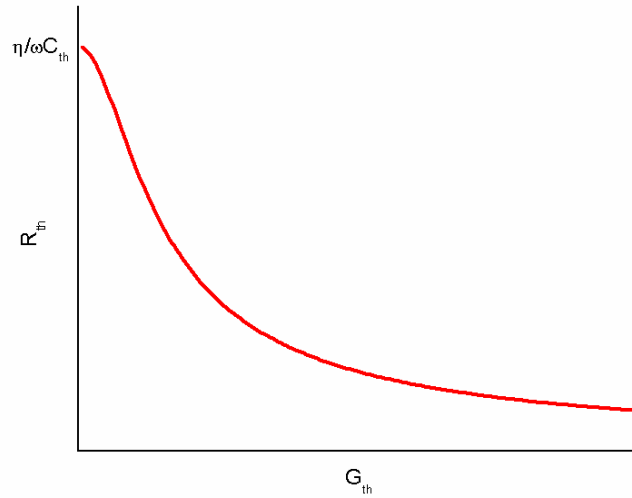


Figure 19. Responsivity (R_{th} [K/W]) vs thermal conductivity (G_{th} [W/K]) in a thermal sensor under sinusoidal illumination power. Clearly, regardless of G_{th} , R_{th} increases with higher absorption (η), lower frequencies (ω), and smaller C_{th} .

Indeed, if thermal conductance were zero the sensor would simply heat up indefinitely from incident radiation. However, real sensors do not have an infinite dynamic range and, of course, Kirchoff's law ensures that radiation losses cannot be avoided [50]. Most thermal sensors are designed such that the unavoidable radiation losses dominate the thermal conductance to maximize sensitivity [10]. Therefore, integrating metamaterials will primarily influence τ and η . Clearly, metamaterials provide η close to 100 %, but τ must be minimized for real time imaging applications, as thermal detectors typically operate in a frequency range where $\omega\tau \ll 1$ to achieve the highest responsivity. Therefore, if τ is large, ω must be small making real time imaging problematic. This means that because G_{th} is already minimized, to minimize τ we must minimize C_{th} . The volume of the materials and their thermal capacitance will determine the total C_{th} . The area of the thermal sensor will be determined by the application and wavelengths of interest; indeed, more sensor area can result in a higher signal from capturing more incident power. The thickness of the thermally sensitive area, however, can be controlled through design and should thus be as small as possible. This is the primary reason for integrating metamaterials into these sensors, the structural materials are poor THz absorbers by themselves [21], [22], and excessively thick structures will perform poorly in a real time imaging setup.

B. BI-MATERIAL SENSOR CHARACTERISTICS

As the previous section illustrates, the basic physics of integrating metamaterials into thermal sensors is similar in that thermal capacitance and absorption are the primary concerns. Of course, each particular sensor will have its own challenges, and the specifics of these challenges for bolometers will be explored in the following chapter. Initially, we chose bi-material sensors to test functionality metamaterials due to the experience of my colleagues in their fabrication and the lab equipment available.

Like all thermal detectors, bi-material sensors respond to a change in temperature of their absorbing element; in this case, the pixel experiences angular deflection per unit power ($d\theta/dP$) and this responsivity can be described as [26]:

$$R = \frac{d\theta}{dP} = R_{th} \frac{d\theta}{dT} = \frac{\eta}{G_{th} \sqrt{1 + \omega^2 \tau^2}} \frac{d\theta}{dT} \quad (6)$$

Clearly, the expression is simply the temperature response of the sensor multiplied by the deflection per unit temperature change (thermomechanical sensitivity). As described before, the thermal time constant limits the speed of the sensor. Noise must also be examined when evaluating performance; in bi-material sensors noise arises from several different sources such as temperature fluctuations, background fluctuations, thermo-mechanical resonances, illumination source fluctuations and the readout system [53]. The first four manifest as fluctuations in the overall sensor deflection, while the readout noise depends on the probing mechanism. In a practical sense, the total noise of the complete detection system can be described by the noise equivalent power (NEP). For bi-material sensors, NEP can be defined as the incident radiant power that produces an angular deflection equal to detector's root mean square (rms) noise [54], [55].

Fundamentally, there are two main choices when designing a bi-material sensor: materials and configuration. Materials should be fabrication-friendly, exhibit low residual stress, have very different thermal expansion coefficients and strong THz absorption. Configurations should have a large absorption area, good thermal isolation to increase sensitivity, provide a reflective surface for optical readout, and have a small thermal capacitance. All of these requirements are intrinsically interdependent making the optimization of the final sensor highly dependent on the intended application. Nonetheless, the quest to achieve high performance THz bi-material detectors starts with $d\theta/dT$, defined by the bimetallic effect, and η , which is maximized by using metamaterial based absorbers. The sensors here were not the first attempted, in our previous work [31] a complex configuration of two fourfold legs metalized in opposite sides were used. Although the total length, and thus bi-material effect, was higher than that of the current design (see Figure 20(a)), the THz sensitive area was half the size to keep the overall pixel size around $200 \times 200 \mu\text{m}^2$. The metallization of the front and back

sides of alternate legs caused the structure to be highly stressed after release. As a result, the sensors were bent as much as 30 degrees out of the substrate plane, which is problematic for the optical readout. The configuration reported here exhibits several advantages, which are highlighted in the next sections.

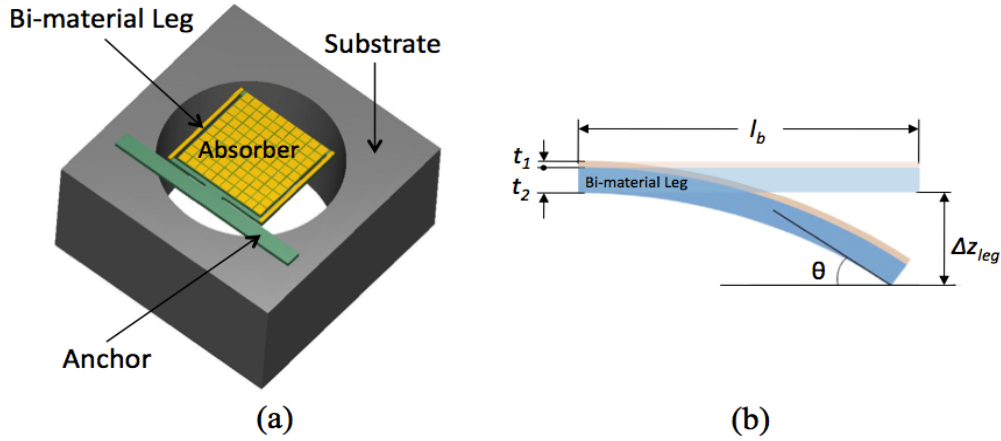


Figure 20. Bi-material sensor. (a) 3D view of the THz bi-material sensor with integrated metamaterial absorber, fabricated on a Si substrate. (b) Close up of an isolated bi-material beam which length is l_b , and metal and dielectric thickness t_1 and t_2 , respectively. Δz_{leg} and $\Delta\theta$ are the linear and angular deflection of the beam, respectively. From [26].

To increase sensitivity, it is important to optimize the bi-material layer thickness to maximize the deflection under increasing temperature. The linear displacement (Δz_{leg}) of the free tip of a bi-material beam, as depicted in Fig. 19(b), was first quantified by Timoshenko [56] and further explored by other groups [53], [57]. If the linear displacement is much smaller than the length of the bi-material beam (l_b), which is true in our case, the angular deflection due to temperature change ($d\theta/dT$) or thermomechanical sensitivity can be estimated using:

$$\frac{d\theta}{dT} = 6l_b (t_1 + t_2) t_2^{-2} \left(4 + 6 \frac{t_1}{t_2} + 4 \frac{t_1^2}{t_2^2} + \frac{t_1^3}{t_2^3} \frac{E_1}{E_2} + \frac{t_2}{t_1} \frac{E_2}{E_1} \right)^{-1} (\alpha_1 - \alpha_2) \quad (7)$$

where t represents thickness, α is the thermal expansion coefficient and E is the Young's modulus. The indices 1 and 2 are used to represent materials 1 and 2, respectively. Table

1 lists some of the most common MEMS materials along with their structural, thermal and electrical characteristics.

When the bi-material legs are connected to a freestanding flat absorber (see Figure 21(a)), the sensor angular deflection is approximately equal to $\Delta\theta$ (see Figure 20(b)). The effect can be further amplified by adding multifold legs with alternate bi-material segments [31]. However, such a configuration also magnifies the bending due to residual stress after release.

Material	Si	SiN _x	SiO ₂	Al	Au
<i>Young's Modulus</i> E ($\times 10^6$ Pa)	100	180	68	70	77
<i>Expansion Coefficient</i> α ($\times 10^{-6}$ K ⁻¹)	2.7	2.1	0.4	25	14.2
<i>Thermal Conductivity</i> g (Wm ⁻¹ K ⁻¹)	130	19	1.4	237	296
<i>Heat Capacity</i> c (J kg ⁻¹ K ⁻¹)	750	691	703	900	129
<i>Density</i> ρ ($\times 10^{-3}$ kg m ⁻³)	2330	2400	2200	2700	19300
<i>Electric Conductivity</i> σ ($\times 10^6$ S m ⁻¹)	-	-	-	10	37
<i>THz refractive index</i> n *	3.48–0.1i	2.1–0.025i	2.0–0.2i	-	-

Table 1. Properties of standard MEMS materials[58], [59]. From [26].

It is clear from Figure 21 that the Al/SiO₂ combination produces the highest sensitivity with the maximum occurring when the metal thickness is approximately one-half of the dielectric thickness. Non-stoichiometric SiN_x can provide less stressed layers than SiO₂ [60], however, silicon-rich SiO_x can be deposited with much lower stress than SiO₂, while preserving most of the thermomechanical and electro-optical properties. During sensor fabrication, testing layers of non-stoichiometric SiO_x and stoichiometric SiO₂ layers with the same thickness were deposited on Si substrates with intrinsic stress

on the order of -13 MPa and -140 MPa, respectively. By selecting SiO_x and Al (both standard MEMS materials), it is possible to maximize $d\theta/dT$ while simultaneously alleviating some of the excessive residual stress related deformation observed in the sensors fabricated in [31]. Furthermore, SiO_x and Al exhibit electro-optical properties that are suitable for highly efficient metamaterial absorbers, as shown in the previous chapter.

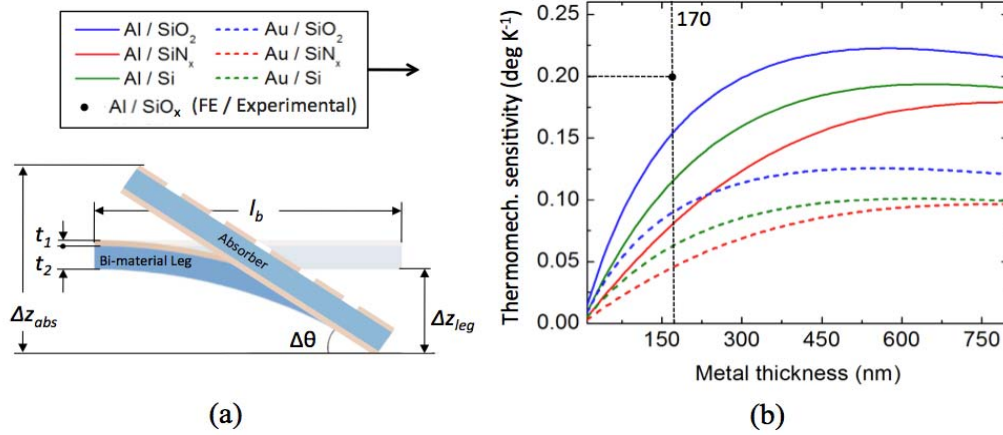


Figure 21. Thermomechanical deflection of the bi-material sensor. (a) Freestanding flat THz absorber connected to a bi-material beam, whose length is l_b , and metal and dielectric thickness t_1 and t_2 , respectively. Δz_{abs} is the total linear displacement and $\Delta\theta$ is the angular deflection of the absorber. (b) Thermomechanical sensitivity ($d\theta/dT$) of the structure of part (a), calculated using Equation (4) for all combinations of metal/dielectric of Table 1 where t_1 varies from 10 to 800 nm and t_2 is fixed in $1.1 \mu\text{m}$. The circular marker shows FE and experimental results for $t_1 = 170$ nm. Solid lines are for Al combinations while dashed lines are for Au. From [26].

C. BI-MATERIAL THZ SENSOR DESIGN

Bi-material terahertz detectors were designed using a metamaterial structure optimized to absorb at 3.8 THz radiation from a QCL available to us. Relatively large pixel dimensions were chosen to increase the absorption area and simplify the fabrication and characterization process. Thermal conductance was intentionally varied among the designs while thermal capacitance remained essentially constant (see Table 2). Figure 22

shows the geometrical details of three sensors (A, B, and C) with different thermal conductances.

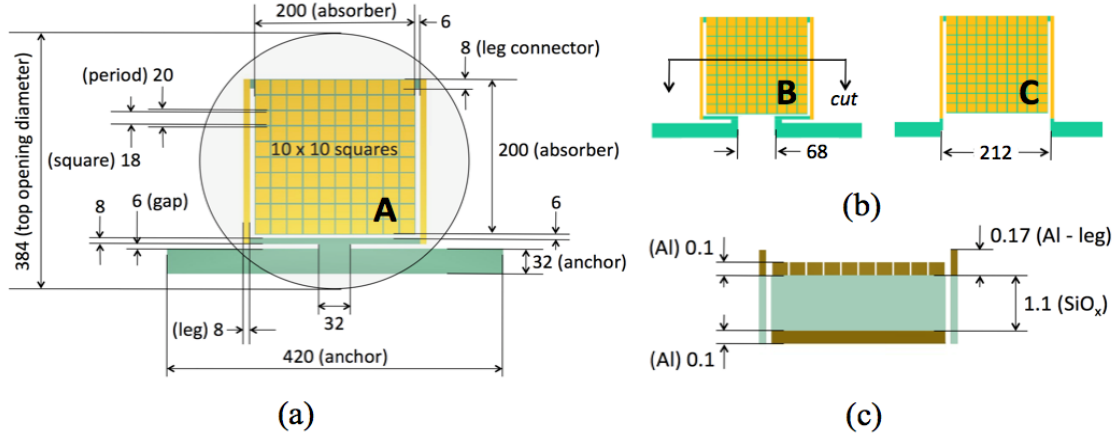


Figure 22. Structural parameters of the three bi-material THz sensors in μm . (a) Top view of sensor A showing all dimensions. (b) Top view of sensors B and C, showing the differences in sizes of the thermal insulator anchors. (c) Vertical cut of the sensor structure. From [26].

The detectors consist of a square metamaterial sensing element in the center connected to two symmetrically located rectangular bi-material legs. The entire structure is then connected to and thermally isolated from the substrate by folded SiO_x anchors with varied dimensions as shown in Figure 22. The thickness of the Al ground plane and squares is 100 nm while the bimaterial legs have a 170 nm layer of Al on the top side. The structural SiO_x is 1.1 μm thick everywhere. The thermal conductance (G) of all the sensors was estimated using the expression:

$$G = \frac{g_{th} A_C}{l} \quad (8)$$

where g_{th} is the thermal conductivity, A_C is the cross-sectional area and l is the length. Since the dimensions of the thermal isolation sections are different, the total thermal conductance was estimated by adding the thermal resistance of each section. The metalized parts are considered thermal shorts due to their high thermal conductivity compared to that of SiO_x . The thermal conductance via radiation loss of heat is found to be an order of magnitude lower than that via the legs due to low emissivity of Al and the

THz metamaterial that cover most of the sensor surfaces. Heat dissipation due to convection is negligible as the sensors typically operate under low pressure (in a vacuum chamber). The thermal capacitance was estimated using the expression:

$$C = c_{th} \rho A_s t \quad (9)$$

where, c_{th} is the material thermal capacity, ρ is the material density, A_s is the surface area and t is the layer thickness. The thermal capacitance of the sensor is the sum of thermal capacitances of the SiO_x and Al layers. The material parameters used for the calculations are given in Table 1. The time constant ($\tau = C/G$) was also estimated for each sensor configuration and listed in Table 2 in addition to other parameters.

Sensor	<i>Sensor A</i>			<i>Sensor B</i>			<i>Sensor C</i>		
Property	<i>Anal</i>	<i>FE</i>	<i>Exp.</i>	<i>Anal</i>	<i>FE</i>	<i>Exp.</i>	<i>Anal</i>	<i>FE</i>	<i>Exp.</i>
<i>Absorptance</i> η	-	0.96	0.95	-	0.96	0.95	-	0.96	0.95
<i>Thermal Conductance</i> G ($\times 10^{-7} \text{ W K}^{-1}$)	1.6	1.7	-	2.2	2.1	-	9.3	8.5	-
<i>Thermal Capacitance</i> C ($\times 10^{-8} \text{ J K}^{-1}$)	11.1	12	-	10.7	12.5	-	9.8	11.9	-
<i>Time Constant</i> τ (s)	0.68	0.7	0.8	0.47	0.6	0.5	0.1	0.14	0.3
<i>Thermomechanical Sensitivity</i> $d\theta/dT$ (deg K^{-1})	0.15	0.19	0.2	0.15	0.2	0.2	0.15	0.25	0.2
<i>Responsivity</i> $d\theta/dP$ ($\times 10^6 \text{ deg W}^{-1}$)	0.95	1.1	1.2	0.65	0.9	0.8	0.15	0.25	0.2
<i>Noise Equivalent Power</i> (due to incident power) NEP ($\times 10^{-9} \text{ W}$)	0.00 5	-	8.6	0.00 6	-	13	0.01 4	-	45

Table 2. THz bi-material sensor analytical, numerical, and experimental parameters. From [26].

The deformation of the sensor with increasing temperature was analyzed using the COMSOL heat transfer module, which allows a uniformly distributed heat flux boundary to be placed at the absorber to emulate the incoming THz power. The anchor attachments to the substrate are fixed and set at a constant temperature to represent the heat sink. All other boundaries are thermally insulated from the surroundings and free to move. The program computes the heat transfer equation at each mesh point allowing the retrieval of several parameters, such as temperature distribution, thermal deformation, etc. For steady state simulations the total incoming heat flux was conveniently set as 1 μW , therefore the thermal deformation and temperature distribution can be directly read “per unit μW .” The angular deformation can be directly obtained by the displacement of the free edges of absorber and hence $d\theta/dT$ can be estimated using the temperature difference between the absorber and heat sink. Also, the responsivity ($d\theta/dP$) of the sensors can be obtained using the maximum deformation (steady state) and the incident heat flux (1 μW). Furthermore, thermal conductance can be estimated using Equation 8.

Time domain simulations were performed to obtain the transient response of the sensor to a pulsed heat flux allowing the retrieval of the time constant of the sensors. Using the obtained time constant and thermal conductance, we estimated the thermal capacitance of the sensors. The calculated and simulated parameters, using the material properties of Table 1, are listed in Table 2 and, in general, show good agreement. Notice that the thermal capacitance values obtained by FE simulations show a small discrepancy as they increase with decreasing sensor mass. This is most likely due to the time constant estimation, which is more susceptible to errors as it decreases. Figure 24(a) and 24(b) show the deformation plots obtained by FE simulation, where the z-axes are scaled up 20 times for visual purposes. The surface color scale indicates the temperature distribution and it is the same for all sensors. It can be seen in Figure 24 that sensor A deflects more compared to sensors B and C under the same incident power (1 μW) primarily due to lower thermal conductance. Figure 24(d) shows the time domain simulations where the sensors are submitted to a step excitation (black solid line) of 1 μW for duration of 8 seconds. The vertical axes show temperature on the left side and angular deflection on the right side.

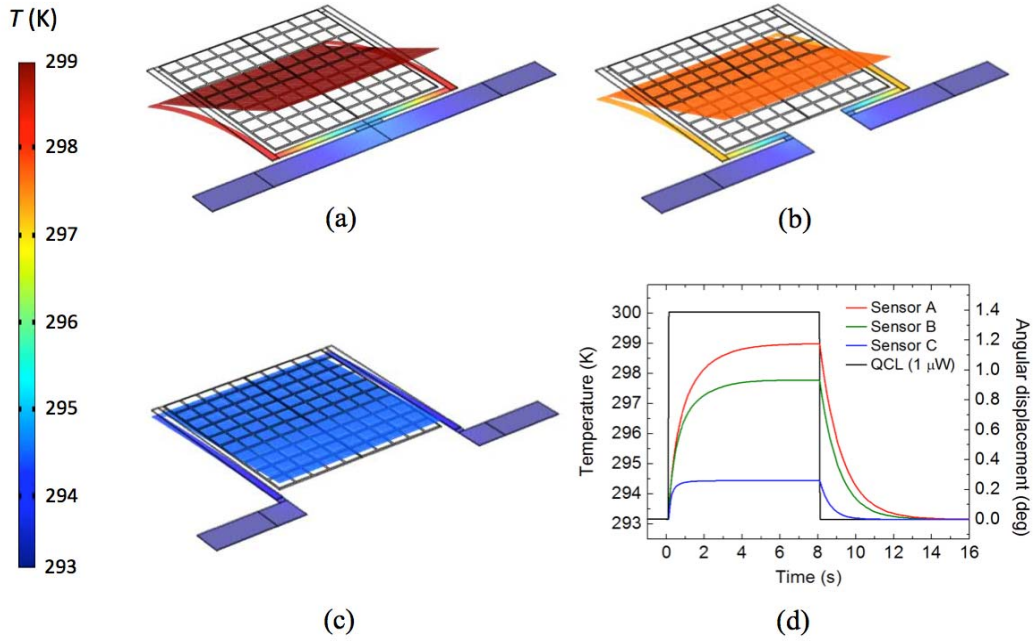


Figure 23. FE simulations showing the deformation plots of sensor A (a), B (b) and C (c) under a constant 1 μW heat flux. The z-axes are scaled up 20 times for visual purposes. The surface colors indicate the temperature distribution according to the color bar on the left. (d) Time domain simulation of all three sensors under a 1 μW step excitation (black line). Temperature change and angular displacement are shown on the left and on the right, respectively. From [26].

Noise sources intrinsic to the detectors were also considered and an analysis similar to that in [53] was performed to determine the NEP. The expressions given by Equations 10 and 11 were adapted from [53] to reflect angular deflection fluctuations. The primary noise sources in thermal detectors are temperature fluctuation, background fluctuation and thermomechanical noises. The spontaneous fluctuation in angular deflection (deg) of the absorbers caused by temperature fluctuations is given by:

$$\langle \delta\theta_{TF}^2 \rangle^{1/2} = \frac{(d\theta/dP)T\sqrt{4k_BGB}}{\eta} \quad (10)$$

where T is the sensor temperature, k_B is the Boltzmann constant, G is the total thermal conductance and B is the bandwidth, which can be set to unity. The background fluctuation noise can be obtained by replacing the total thermal conductance in Equation 10 by thermal conductance via radiation loss of heat. However, this is much smaller than

the thermal conductance via the legs and its contribution to noise can be neglected. The angular deflection (deg) due to thermomechanical noise, knowing that the detector operating frequency is much slower than the mechanical resonances (few kHz), is given by:

$$\langle \delta\theta^2_{TM} \rangle^{1/2} = \frac{360}{\pi l_b} \sqrt{\frac{4k_B GB}{Qk\omega_0}} \quad (11)$$

where Q is the quality factor, k is the stiffness and ω_0 is the resonant angular frequency of the mechanical structure. Using the eigenfrequency solver in the COMSOL structural mechanics module, the first resonant frequency and stiffness of all the sensors were estimated and found to have values 3.5, 4.0 and 6.0 kHz and 0.02, 0.025 and 0.04 Nm^{-1} for sensors A, B and C, respectively. Typical Q values for similar structures lie between 100 and 1000 in vacuum [53]. The noise was estimated and as expected, the dominant source is the temperature fluctuation in the detector. The total noise intrinsic to the sensors was estimated to be 5.0, 4.0 and 2.0 μdeg . The NEP values of the three sensors were calculated by dividing the fluctuations due to the noise by their respective responsivities, and are listed in Table 2.

D. FABRICATION AND CHARACTERIZATION

The sensors were fabricated using standard micromachining technology. First, a 100 nm thick aluminum (Al) film was deposited on a 300 μm thick silicon (Si) substrate by e-beam evaporation. Then, the Al layer was patterned and wet etched to form the absorber ground plane. Next, a 1.1 μm thick SiOx layer was deposited using plasma enhanced chemical vapor deposition (PECVD) at 300 $^{\circ}\text{C}$, followed by another 100 nm thick Al film. The second Al layer was then patterned and plasma etched to define the absorber metamaterial squares. Then a 170 nm thick Al layer was deposited, patterned and lifted off to form the bi-material legs. The sensor structure was then created by reactive ion etching of the SiOx layer. Finally, the structures were released through backside trenching using the Bosch etch process. Circular openings were chosen to ensure release of the structure and to help refine the Bosch etch recipe. Figure 24(a) and

24(c) show the optical profile of the fabricated sensor A along with micrographs of the three sensors and an array of sensors of type A.

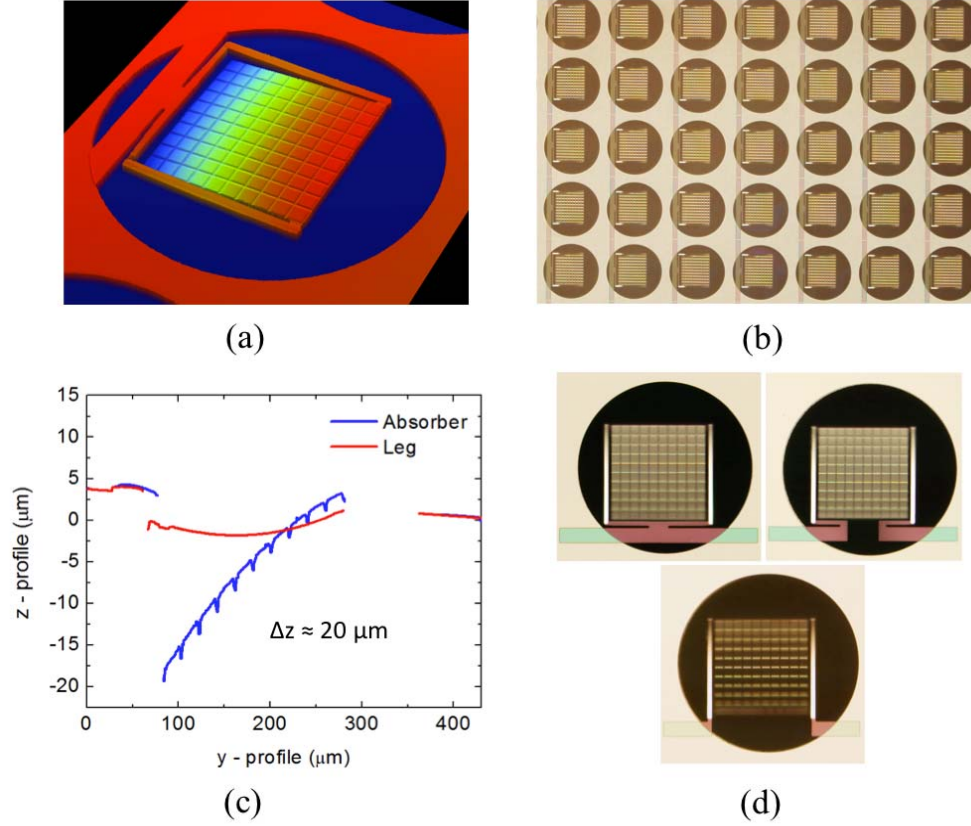


Figure 24. Fabricated THz bi-material sensors. (a) 3D optical profile of sensor A (the aspect ratio is preserved). (b) Micrograph of an array of sensor A. (c) 2D profile taken along the bimaterial legs direction (y-profile) with the processing direction (z-profile) scale exaggerated to show the residual deflection of the legs (red line) and absorber (blue line). (c) Micrographs showing the top view of sensors A, B and C. From [26].

The 3D profile in Figure 24(a) is an actual view of sensor A while the 2D profile in Figure 24(c), taken along the bi-material legs direction (y-profile), is exaggerated in the processing direction (z-profile) to show the residual deflection of the legs and absorber of the sensor. The measured residual deflection of the absorber is approximately 6° for the sensors A and B and 8° for sensor C. It is easy to observe that the absorber is almost flat due compensation of stresses from the aluminum layers in both sides of the

SiOx layer. Due to the deflection of the sensors, micrographs shown in Figure 24(d) are not completely focused across the surface. In addition to the sensors, the fabricated wafer contains an area of $10 \times 10 \text{ mm}^2$ filled with the same metamaterial structure used in the sensors. This is to allow accurate measurement of the absorption characteristics of metamaterial used in the sensors. The absorptance of the metamaterial film was measured as described in chapter II and compared with the QCL emission characteristics as shown in Figure 25(a). A good match between the absorptance peak position of the metamaterial and the 3.8 THz QCL emission frequency was achieved with nearly 90% absorptance. This assured that the sensors absorbed our QCL emission with high efficiency.

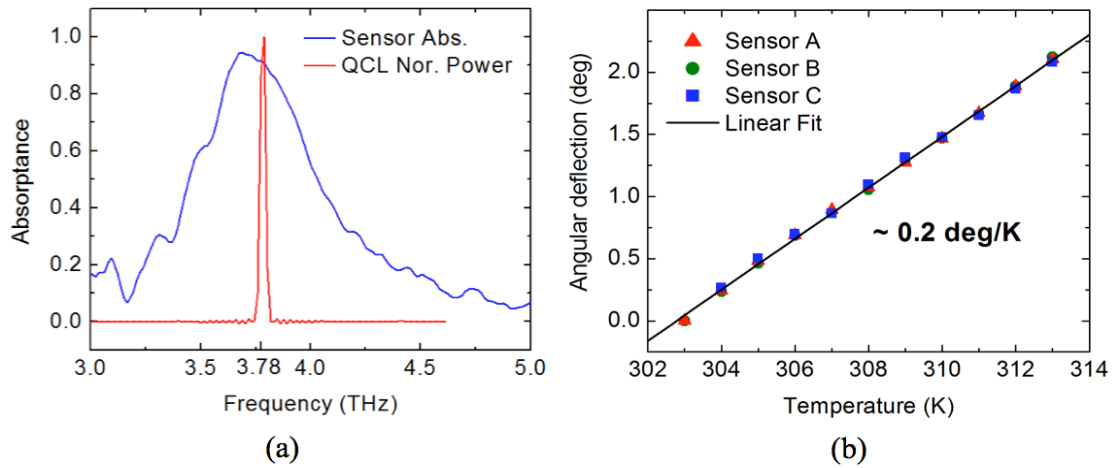


Figure 25. (a) Measurement of the absorptance spectra of the THz sensors metamaterial structure (blue line) compared with the QCL normalized emission (red line). (b) Measured angular deflection (markers) upon temperature change. Notice that the effect is linear and almost indistinguishable among the sensors, resulting in approximately 0.2 deg/K thermomechanical sensitivity. From [26].

Next, the thermal response of the sensor ($d\theta/dT$) was measured. The temperature gradient in the bi-material section of the leg was estimated to be less than 5% of that between the central absorbing element and the substrate. Thus, the bi-material section of the leg can be treated as thermally shorted allowing the measurement of the thermal response by uniformly heating the sensor. The measurement was performed by attaching the sensor to a flat resistive heating element and sweeping the temperature from 303 to

313 K. The reflection of a laser diode beam from the backside of the sensor's ground plane was projected on a screen and the angular deflection of the sensor was determined. Angular deflections from the three sensors are shown in Figure 25(b) with different markers. The deflections are almost indistinguishable because the detectors have the same bi-material leg dimensions. The solid line is a linear fit, showing that the response in this temperature range is linear and approximately 0.2 deg/K, which is slightly higher than the estimated values (see Table 2 and Figure 21). Figure 21 shows that the thermal response of the sensors can be further increased by, for example, decreasing the SiO_x thickness or increasing the Al thickness on the legs. Test structures fabricated in parallel with these sensors showed that increasing the Al thickness on the legs also increases the residual stress. Decreasing the dielectric thickness has a similar effect in addition to reducing absorber efficiency [30]. Further tuning of the fabrication process is necessary to reduce the residual stress on the bi-material legs to decrease the initial bending as depicted in Figure 7(a).

Subsequently, the sensors were placed in a vacuum chamber and operated at a pressure of approximately 0.03 mTorr to minimize the heat loss by convection [52]. The QCL was kept inside a cryostat and operated at around 15 K. The divergent THz beam passed through the cryostat Tsurupica window and the radiation was focused by a 40 mm polyethylene lens onto the sensors. Both Tsurupica and polyethylene exhibit reasonable transmission (~65%) in the THz range. The QCL was operated in pulsed mode with the pulse width fixed at 5 μ s and a variable pulse rate to control the output power. The deflection of the sensor was measured using the same procedure described earlier for a set of QCL pulse rates ranging from nearly zero to 5 kHz. The absolute power that reaches the sensors (incident power) is estimated using the responsivity ($d\theta/dP$) in Equation 6 along with the calculated thermal conductance and measured absorptance. Note that the QCL switching frequency and duty factor must be taken into account since the sensors can only respond to the average power. Figure 26(a) shows the measured angular deflection versus incident power for all three sensors (colored markers). For all of the sensors, the responsivity values estimated analytically tend to be lower than that of the FE and experimental values mainly due to the underestimation of bimetallic effect

$(d\theta/dT)$, by Equation 7 (see Figure 21). As expected from Equation 6, responsivity of the sensors was found to decrease with increasing thermal conductance.

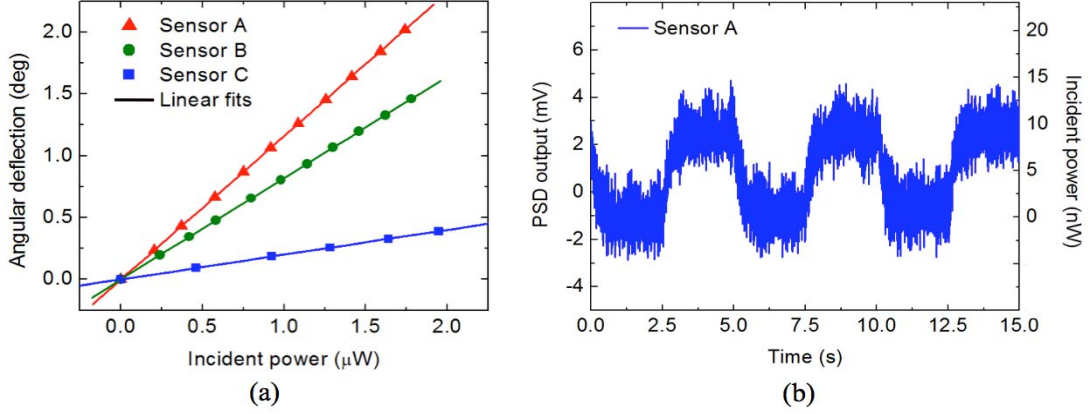


Figure 26. Responsivity and NEP measurements. (a) Measured angular deflection per varying incident power for all three sensors (colored markers) Notice that responsivity increases as thermal conductance decreases. (b) Measured output voltage of the PSD for sensor A by gating the QCL output at 200 mHz. The power incident in the detector is shown on the right vertical axis. From [26].

To determine NEP, a position-sensing detector (PSD) was added to the experimental setup to read the deflection at low power levels. The NEP was then measured for each detector and listed in Table 2. Figure 26(b) shows measured output voltage of the PSD for sensor A by gating the QCL output at 200 mHz. It is important to highlight that the measurements include the effects of QCL power fluctuations and optical readout noise, not considered in the theoretical estimations discussed earlier. The difference between the measured values (3 orders of magnitude higher) and the estimated ones (Table 2) can be attributed primarily to the readout noise. The QCL power fluctuations [61] do not seem to contribute to the observed noise since the noise floor when the QCL is off, shown in Figure 26(b), is similar to the noise observed when the QCL is on. As expected, NEP increases from sensor A to C due to decrease in responsivity. The measured NEP values, including the readout noise and the intrinsic noise of the sensor, can be translated into minimum detectable temperature difference on the sensor, found to be approximately 50 mK for all three sensors. This value is similar to those of bi-material sensors operating in the IR range [53], [58].

The time domain response was also measured using the PSD and the results for the three sensors are shown in Figure 27(a) under the same incident power with the QCL gated at 500 mHz. As observed in Figure 26, sensor A is more sensitive, which agrees with the predictions and previous measurements. Since the sensors have the same η , the same absorbing area, same materials, the same $d\theta/dT$, and nearly the same thermal capacitance, speed and responsivity are completely controlled by the thermal conductance, which depends on the anchor geometry.

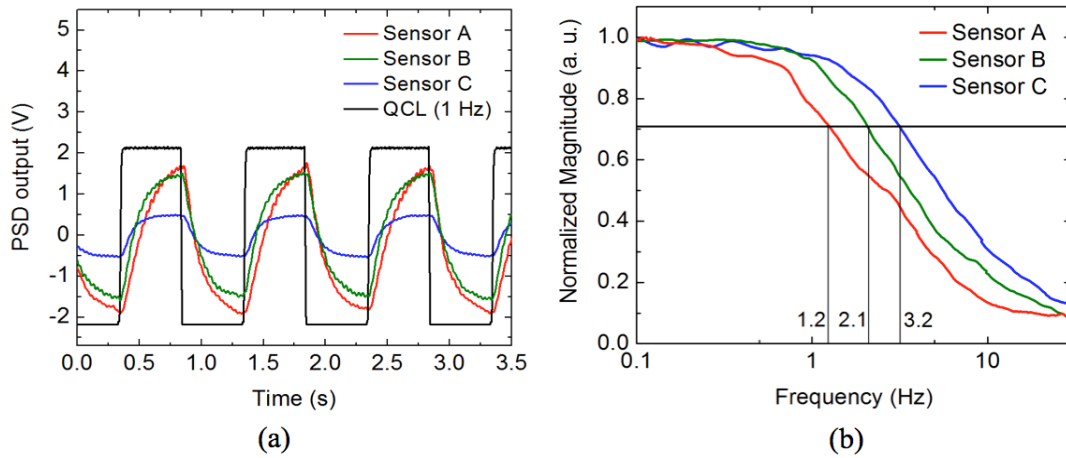


Figure 27. Time and frequency domain measurements. (a) Time responses of sensors A, B and C measured under the same incident power with the QCL gated at 1 Hz. Noticed that sensor A is more sensitive and slower, which agrees with the predictions and previous measurements. (b) Normalized frequency responses for the three sensors (colored lines). The time constants were retrieved by taking the inverse of the 3 dB frequencies that are 1.2, 2.1 and 3.2 rad/s for sensor A, B and C, respectively. From [26].

The time constant of the sensors was determined by sweeping the QCL gating frequency from 50 mHz to 30 Hz and recording the PSD peak to peak voltage. The normalized frequency responses for the three sensors are shown in Figure 10(b). The time constants were retrieved from Figure 27(b) by taking the inverse of the 3 dB frequency and included in Table 2. In general, the measured time constants agree well with the FE estimations, while the analytical approach underestimates this parameter. The sensors are, apparently, slow for real time imaging; however, pixel size can be reduced to increase the speed of operation. A tradeoff between speed and sensitivity has to be made according to

specific applications. Although the fabricated sensor arrays do not have high spatial resolution, their imaging capabilities were probed by a CCD camera with coaxial illumination as schematically illustrated in Figure 28(a) [62], [63]. An image of the QCL beam, gated at 500 mHz, is shown in Figure 28(c) compared with the same image obtained using a commercial IR microbolometer camera with THz optics [64] (Figure 27(b)). The focal plane array of the IR camera has 30 μm pitch of and can resolve the rings associated with the QCL beam. Our sensor array, on the other hand, has a 430 μm pitch and cannot resolve the rings; nevertheless, it gives a raw image that clearly shows where the energy is concentrated and the circular shape of the THz beam. Finally, it is possible to optimize THz bi-material sensor configuration, size, fabrication processes and readout to achieve real time imaging.

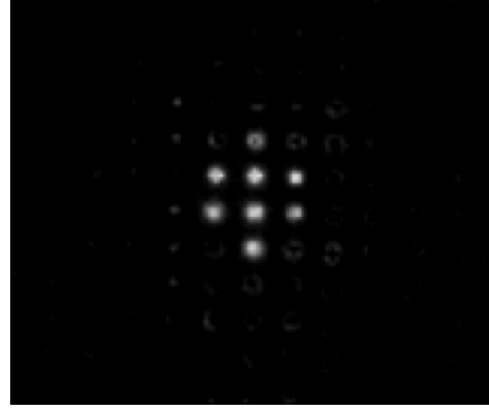
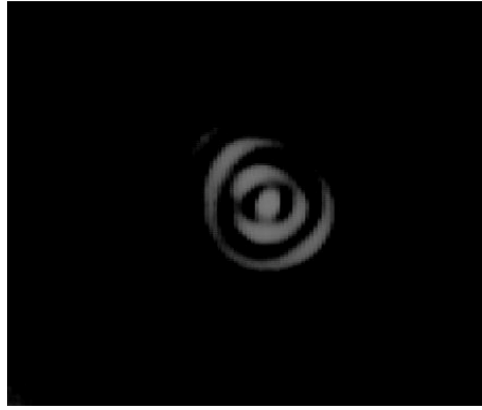
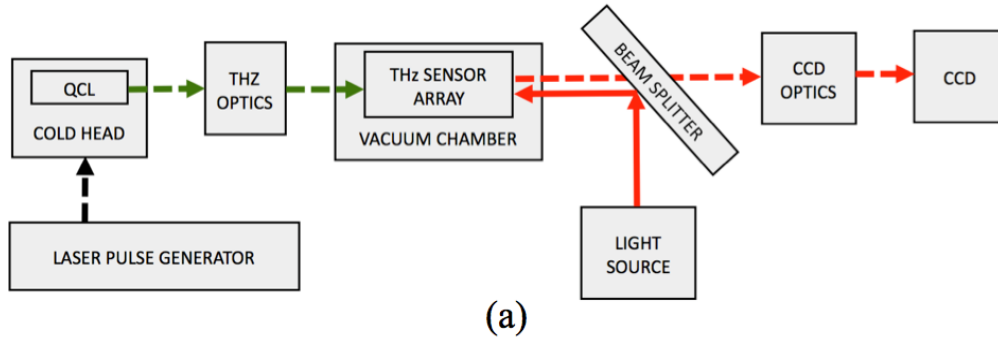


Figure 28. QCL beam imaging. (a) Optical readout used to record videos [46] and the snap shot showed in part (c). The images were recorded using background subtraction to suppress to the effects of the residual stress of the sensors. (b) Image obtained using a 30 μm pitch commercial IR microbolometer camera with THz optics. (c) Image (Media 1) of the same QCL beam, gated at 500 mHz, obtained using an array of sensor A with 430 μm pitch using the readout depicted in part (a). Notice that since the pitch of our sensor are one order of magnitude higher than the IR camera, it cannot resolve the rings associated with the QCL beam, showed in part (b). From [26].

THIS PAGE INTENTIONALLY LEFT BLANK

IV. INTEGRATING METAMATERIALS INTO MICROBOLOMETER PIXELS

Note: *Other than the last section, this chapter is published practically unaltered in Optical Materials Express [25].*

A. CHALLENGES TO BOLOMETER INTEGRATION

As the previous chapters have described, metamaterials can make effective thin THz absorbers for thermal sensors. Bi-material sensors demonstrated in Chapter III the metamaterial THz absorber and bi-material legs are physically separated and do not interfere with each other's function. In the case of microbolometers, a temperature sensitive layer must be included in the central absorbing area, or microbridge which can affect the efficiency of the metamaterial absorber. This resistive bolometric layer can be made out of several different materials, such as titanium (Ti) and vanadium oxides (VO_x). In Chapter III, it was shown that the absorbing layers should be as thin as possible to reduce thermal capacitance (C_{th}), and thus the thinnest choice would be one in which the bolometric layer is simply integrated into the middle of the dielectric spacer as in Figure 29 or serve as the ground plane of the metamaterial. Unfortunately, the latter option leads to a significant reduction in absorption as THz will easily penetrate high resistivity bolometric materials and thus defeats the purpose. Therefore, the former option was investigated, although some other possible configurations will be examined.

B. FABRICATION AND MEASUREMENT

The approach used in this work involves a metamaterial structure with a bolometric layer embedded in the dielectric layer as schematically illustrated in Figure 29. The aim of the work in this chapter is to determine the optimal location of the bolometric layer within the dielectric to achieve the highest possible THz absorption. Three wafers containing metamaterial absorbers with Ti as the bolometric layer located in the dielectric spacer at varying depths along with one without a bolometric layer were fabricated using standard MEMS microfabrication techniques, similar to those used in Chapter II. The fabrication sequence includes deposition of an 85 nm thick layer of Al on

4" Si substrates using e-beam evaporation. Following this, a layer of low stress nonstoichiometric silicon-rich silicon oxide (SiO_x) with different thicknesses was deposited using plasma enhanced chemical vapor deposition (PECVD).

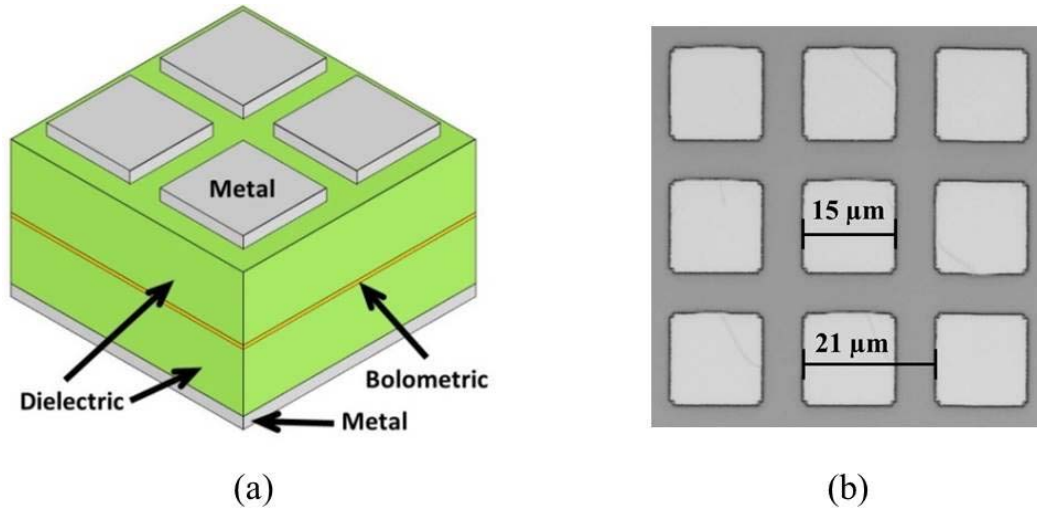


Figure 29. Schematic (a) and top view micrograph (b) of a metamaterial absorber with a bolometric layer embedded in the dielectric. The square size and pitch were selected to have an absorption peak within the 1–10 THz band. From [25].

Wafers A-D possessed 1270 nm, 765 nm, 297 nm, and 1590 nm of SiO_x , respectively, confirmed through optical interferometry. Then, a Ti layer was sputter deposited using Ar plasma onto wafers A-C and a Si test wafer with a SiN_x isolation layer to measure conductivity. The measured thickness of Ti was found to be about 10 nm and confirmed to have a sheet resistance of about 220 Ω/sq , which corresponds to conductivity of $4.45 \times 10^5 \text{ S/m}$. Following the deposition of Ti, an additional SiO_x layer with thicknesses of 297 nm, 765 nm, and 1270 nm were deposited using PECVD on wafers A-C, respectively. This resulted in nearly equal total spacer thicknesses, including Ti layer, of 1577 nm, 1540 nm, 1577 nm, and 1590 nm for wafers A-D. A second 85 nm thick layer of Al was then deposited onto wafers A-D using e-beam evaporation and was then patterned using photolithography and sputter-etched with Ar plasma to form an arrays of squares as in Chapter II, with the absorption characteristics of the 15 μm side and 21 μm pitch configuration shown here.

As described in Chapter II, square size mainly influences the resonant absorption frequency, while dielectric thickness and periodicity strongly affects absorption magnitude. This particular configuration was chosen for its resonant frequency in the 1–10 THz range, and other configurations with varying resonant frequencies can be found in Chapter II. All wafers were intentionally over-etched approximately 150 nm into the SiO_x to assure complete insulation between square elements. The composition of layers of wafers A-D are summarized in Table 3. To determine the optical properties of these metamaterial absorbing layers in the THz spectral range, reflection measurements were taken using a Thermo-Nicolet Nexus 870 Fourier Transform Infrared Spectrometer (FTIR) with a globar source and PIKE Technologies MappIR accessory. An Au-coated Si wafer was used to establish the background for the reflectance measurements. The two 85 nm thick Al layers block any significant transmission due to the 40 nm skin depth at around 4.7 THz, resulting in over two orders of magnitude reduction of power due to exponential attenuation. The periodicities used are less than one third of the free space wavelength, resulting in negligible higher order scattering [43]. As before, this allows $A+T+R=1$ to be simplified to $A \approx 1-R$. The resulting absorption spectra for samples A-C are plotted in Figure 30(a).

Wafer	<i>Top SiO_x</i>	<i>Bottom SiO_x</i>	<i>Total Spacer^a</i>	<i>Max. Absorption^b</i>
A	297	1270	1577	62%
B	765	765	1540	88%
C	1270	297	1577	94%
D	----	----	1590	98%
^a Includes 10 nm of Ti. ^b For 15 μ m squares with 21 μ m periodicity				

Table 3. Thickness of the dielectric spacer layers (in nm) of each sample. From [25].

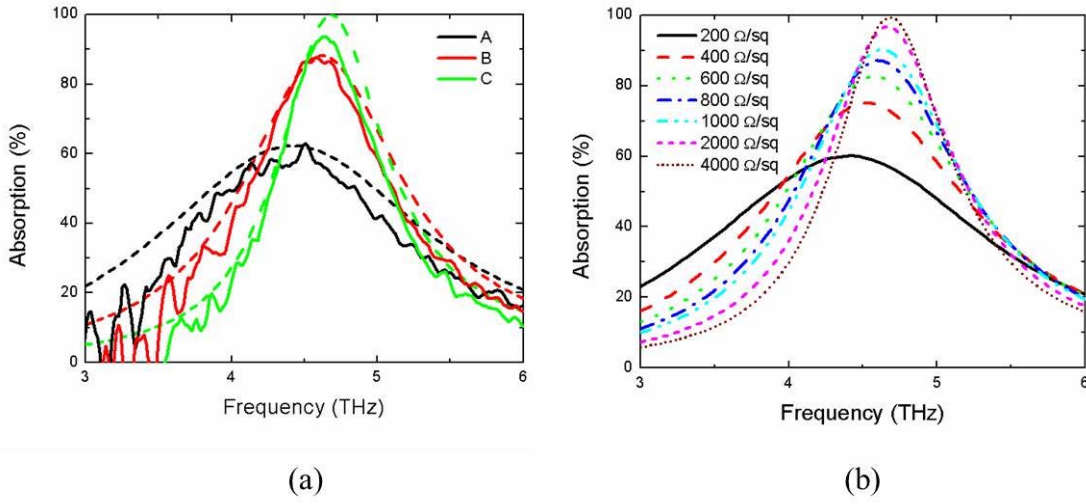


Figure 30. (a) Experimental (solid) and FE model (dashed) absorption spectra for samples A (black), B (red), and C (green). (b) Theoretical absorption curves for sample A for a set of sheet resistivities in the bolometric layer. Square size is $15\ \mu\text{m}$ with $21\ \mu\text{m}$ periodicity for both plots. From [25].

C. RESULTS AND DISCUSSION

It is clear that in Figure 30(a), as the Ti conductive layer gets closer to the patterned top Al layer, the THz absorption of the metamaterials is significantly reduced and slightly red shifted. This is expected conceptually as the Ti layer would function as a poor ground plane if the lower SiO_x and Al layers were removed. The redshift in the resonant absorption frequency is larger than the frequency shifts observed in Chapter II for thinner dielectric thicknesses, suggesting that a simple reduction of dielectric thicknesses will not explain these absorption spectra. To model the THz absorption characteristics of the metamaterial film with an embedded bolometric layer, finite element (FE) simulations were performed using the RF module of COMSOL multiphysics software explained in greater detail in Chapter II. The periodic geometry of the metamaterial absorbing film allows for a single unit cell to be modeled with periodic boundary conditions. Internal ports or scattering boundary conditions allow incoming plane waves at specific frequencies to enter the model. The THz absorption can be calculated by subtracting off reflection and transmission coefficients calculated from the S parameters. Alternatively, resistive heating can be used to calculate absorption. This

method is especially useful for calculating the absorption of elements that are not thermally linked, such as a ground plane disconnected from a bolometer microbridge. The aluminum layers were modeled using a conductivity of 1×10^7 S/m, confirmed through four-point probe and stylus profilometer measurements. SiO_x was modeled as a dielectric with a complex index of refraction of $1.95 + 0.025i$, adjusted from the SiO_2 values used in Chapter II based on the experimental results therein. Ti was modeled as having a sheet resistance of $220 \Omega/\text{sq}$ based on four-point probe measurements. The exact thickness of the Ti is irrelevant as long as the sheet resistance is well known [48] and was estimated at 10 nm from previous depositions. As in Chapter II, the over-etching of SiO_x is included in the models, producing a slight blue shift in the resonant absorption frequency due to an effectively smaller index of refraction. Figure 30(a) shows the comparison of simulated and measured data for the three samples. The simulated data is able to capture the effect of the location of Ti layer on the absorption reasonably well. E-field magnitude plots for these simulations are shown in Figure 31, all using the same color scale for E-field intensity.

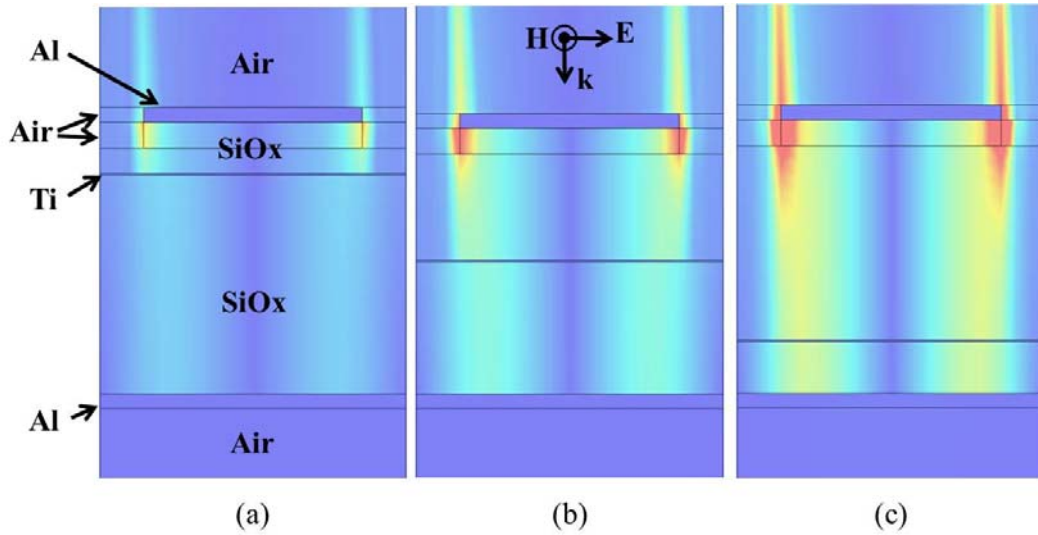


Figure 31. E-field magnitude plots from COMSOL FE simulations of $15 \mu\text{m}$ squares with $21 \mu\text{m}$ pitch at 4.7 THz for samples A (a), B (b), and C (c). All plots use the same color scale, with warmer colors indicating more intense E-fields. Material types of different regions are labeled in (a). E-field, H-field, and propagation vectors of the incident THz waves are shown on (b). From [25].

It is clear that the E-fields do penetrate the Ti layer but not the ground plane in all cases, and that the Ti is indeed acting as a poor ground plane. The E-fields also become less intense as the Ti layer nears the square array, indicating that it is negatively affecting the resonance. In addition, absorption of sample A is also simulated for a set of conductivities of the bolometric layer as shown in Figure 30(b). It can be seen that, if the conductivity of this layer is reduced, the influence of the layer on the absorption of the metamaterial decreases, as expected. Since typical high TCR bolometric layers have sheet resistances in the $k\Omega$ range, we should expect that a spacer of 300 nm of SiO_x between the bolometric layer and the patterned Al layer will be sufficient for achieving high THz absorption. The results indicate that the two most important parameters that affect the absorption peak height are the conductivity and position of the bolometric layer between the patterned Al layer and ground plane of the metamaterial. The data in Figure 30 also seems to show that within the range of parameters used, there is some equivalence in the effects of sheet resistance and position of a thin bolometric layer on the absorption spectrum. Qualitatively, less conductive layers should allow for greater penetration of E-fields and thus more of the desirable resonance between the square array and the ground plane. Also, a high conductivity layer near the ground plane or a low conductivity layer near the square array should both converge to the original absorption spectrum.

D. OTHER POSSIBLE CONFIGURATIONS

Now that we have established that the impact on absorption is reduced as the sheet conductivity is reduced and as it is moved closer to the ground plane, we can evaluate other possible configurations investigated by other researchers as depicted in Figure 32. Maier et al. fabricated a structure analogous to Figure 32(a) [65] and Figure 32(c) [32] for the mid-IR range (3–8 μm) range. They note that the bolometric layer, in their case polysilicon (poly-Si), interfered with their metamaterial significantly for the configuration in Figure 32(c). Certainly, the configuration in Figure 32(a) eliminates interference between metamaterial and the bolometric layer since they are optically separated since the ground plane permitting no significant THz transmission. However, when comparing THz metamaterials to mid-IR metamaterials, an important distinction

emerges. Note that in Chapter II, the optimal dielectric thickness for high THz absorption was approximately 1 μm , while in the case of Maier et al. the optimal dielectric thickness can be as thin as 250 nm [65] also seen in other similar work [42]. Thus, the configuration in Figure 32(a) is not suitable for THz applications due to increase of thermal capacitance when extra layers added for separating the bolometric layer.

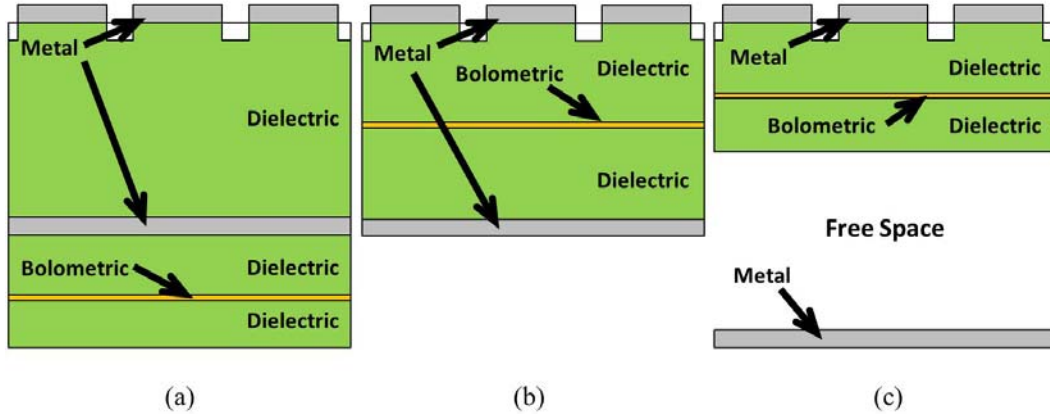


Figure 32. Three possible configurations for integrating a conductive layer into a THz absorbing metamaterial using a metal, bolometric layer, and a dielectric with the bolometric layer below (a) and within (c) the metamaterial layer. Configuration (c) thermally disconnects the ground plane. The configuration we used is shown in (b) with Ti.

Of course, thickness can be reduced with some loss in absorption if required and controlled over-etching can eliminate some of the dielectric spacer. However, these methods will still reduce the performance of the microbolometer pixel; this is why the configuration in Figure 32(b) was emphasized for THz metamaterials in addition to the fact that, as with the bi-material pixels, the metal layers on both sides of the dielectric will compensate for each other in terms of residual stress. The structure depicted in Figure 32(c) does present an interesting opportunity, albeit with some fabrication challenges. In this configuration, the thickness of the metamaterial absorbing layer *includes* the air gap thus allowing the thermal capacitance of the microbridge to be relatively small. The issue here is shown in Figure 5 in Chapter II, the FE model indicates that the ground plane has a non-negligible power dissipation of over 20% of the absorbed

THz at the resonant frequency. As the dissipation in any material will depend on the electric field and conductivity or complex refractive index of that material (assuming magnetic losses are negligible), it should be possible to effectively control where the absorption occurs. Indeed, if the ground plane were constructed out of a material with a high THz conductivity, dissipation in that layer would be less than the other layers, minimizing this problem. Therefore, while the structure in Figure 32(b) is likely the safest configuration to fabricate microbolometers with high performance, Figure 32(c) would allow for an even smaller thermal capacitance.

V. CONCLUSION

The research presented here demonstrates the ability of metamaterials to enhance thermal sensors operating in the THz region of the spectrum by improving their absorption characteristics. Finite element models provided key insight leading to fabricated metamaterial absorbers and bi-material sensors that performed well in the 3–8 THz range.

The THz metamaterial absorbers, composed of a metal layer patterned into a periodic array of squares separated from a ground plane of continuous metal by a dielectric spacer were found to have nearly 100% absorption at a specific THz frequency. The peak absorption frequency was inversely proportional to the dimension of the squares. In addition, metamaterial THz absorbing layers with one, two, and three absorption peaks we fabricated using complex unit cell structures instead of single square unit cells. The use of standard microfabrication materials, Al and SiO_x for the fabrication of metamaterials, allows them to be incorporated into the construction of thermal sensors such as microbolometers or bi-material sensors. The results indicate that these metamaterial absorbers can be used as absorbing layers in thermal imagers paired with narrow-band sources to significantly enhance their sensitivity through resonant absorption at the emitter frequency. In addition, dual- and triple-band configurations can be used with multiple lasers or broader sources, as desired.

The metamaterials were successfully integrated into bi-material pixels. Sensor materials and configurations were chosen in order to maximize responsivity. The combination of favorable thermal, mechanical and optical properties of the MEMS fabrication-friendly materials SiO_x and Al were advantageous. Analytical and FE models were used to predict the performance of the sensors. A highly efficient metamaterial structure was developed to provide near 100% absorption at 3.8 THz while simultaneously serving as a structural layer and providing access for external optical readout. The fabricated sensors showed responsivity values as high as 1.2 deg/μW and time constants as low as 200 ms, depending on the configuration. Minimum detectable power on the order of 10 nW was observed, demonstrating that the sensors can operate

with low-power THz sources. Although the sensors were not optimized for imaging, the use of an external optical readout allowed us to obtain raw images of the QCL beam indicating the potential of these detectors to be further optimized for use in focal plane arrays for real time THz imaging. The successful design, fabrication, and characterization of bi-material MEMS sensors, using metamaterial absorbers demonstrates the potential of this approach for THz imaging.

The final phase of the research, fabrication of THz-absorbing Al/SiO_x/Al metamaterial layers with a thin Ti conductive layer inserted into the dielectric spacer to be used as bolometric layer was explored. The introduction of Ti reduced the magnitude of the absorption peak when placed near the patterned Al layer in addition to a small redshift. The measured absorption spectra are in reasonably good agreement with those of the simulations. The results indicate that the bolometric layer should be placed near the ground plane for achieving maximum absorption. FE simulations of the effects of the bolometric layer on absorption suggest weak position sensitivity when the sheet resistance of the bolometric layer exceeds about 1 k Ω /sq. The findings indicate that metamaterial THz absorbers should be able to improve the performance of microbolometer cameras in the THz range without compromising their thermal time constants.

A. FUTURE WORK

The knowledge gained in this work can prove useful for the fabrication of microbolometer pixels with integrated THz metamaterial absorbers. Therefore, the next step in this research should be the fabrication and characterization of microbolometer pixels using the optimized metamaterials with embedded bolometric layers for THz imaging. To detect a change in resistance in a microbolometer pixel, a Wheatstone bridge is employed in readout systems [10] as illustrated in Figure 33. To ensure the load resistors are of similar resistance, they can simply be other microbolometer pixels that are at ambient temperature. Self-heating is an inevitable issue with a microbolometer readout, given that any power dissipated while probing the Wheatstone bridge will change the resistance of the microbolometer pixels. Therefore, a possible configuration

illustrated in Figure 33 has two thermally shorted pixels, one pixel that is blind to THz by joining the squares together (but maintains the same thermal capacitance as the sensitive pixel).

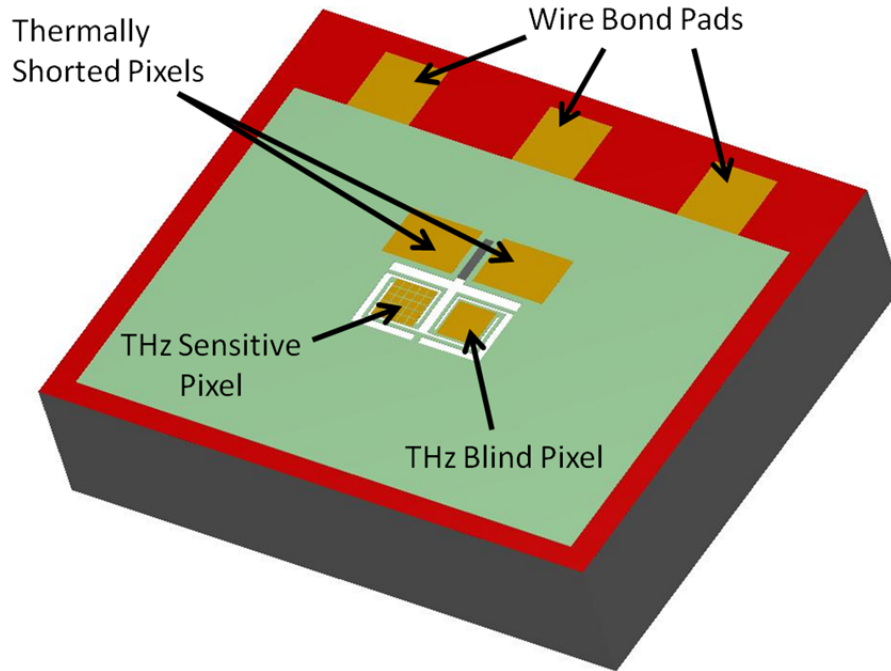


Figure 33. Wheatstone bridge configuration for THz metamaterial microbolometer characterization. The thermally shorted pixels are not released from the substrate and the blind pixel has a single metal square instead of the patterned layer and thus will not absorb THz efficiently, but will have essentially the same thermal properties as the sensitive pixel. Several Wheatstone bridges are fabricated together, their common ground is not visible.

This configuration will automatically cancel much of the self-heating, allowing for an easier readout. Additionally, a separate configuration with three thermally shorted pixels and one sensitive pixel can be used to evaluate the self-heating during readout. In commercial systems, an array can be read out pixel by pixel with the same Wheatstone bridge, but such readout systems require more fabrication steps to incorporate the necessary electronics.

THIS PAGE INTENTIONALLY LEFT BLANK

LIST OF REFERENCES

- [1] R. H. Clothier and N. Bourne, “Effects of THz exposure on human primary keratinocyte differentiation and viability,” *J. Biol. Phys.*, vol. 29, no. 2–3, pp. 179–185, 2003.
- [2] “CIRCE: Filling the THz Gap,” *CIRCE: Coherent InfraRed Center at the ALS*, <http://circe.lbl.gov/THzGap.html>
- [3] J. F. Federici et al., “THz imaging and sensing for security applications—explosives, weapons, and drugs,” *Semicond. Sci. Technol.*, vol. 20, no. 7, pp. S266–S280, 2005.
- [4] S. M. Kim et al., “Biomedical terahertz imaging with a quantum cascade laser,” *Appl. Phys. Lett.*, vol. 88, no. 15, p. 153903, 2006.
- [5] Z. D. Taylor et al., “Reflective terahertz imaging of porcine skin burns,” *Opt. Lett.*, vol. 33, no. 11, pp. 1258–1260, 2008.
- [6] K. Fukunaga et al., “Real-time terahertz imaging for art conservation science,” *J. Eur. Opt. Soc. Rapid Publ.*, vol. 3, p. 08027, 2008.
- [7] A. A. Gowen et al., “Terahertz time domain spectroscopy and imaging: emerging techniques for food process monitoring and quality control,” *Trends Food Sci. Technol.*, vol. 25, no. 1, pp. 40–46, 2012.
- [8] A. G. Davies and E. H. Linfield, “Bridging the terahertz gap,” *Phys. World*, vol. 14, pp. 37–41, 2004.
- [9] M. S. Grace et al., “The Python pit organ: imaging and immunocytochemical analysis of an extremely sensitive natural infrared detector,” *Biosensors and Bioelectronics*, vol. 14, no. 1, pp. 53–59, 1999.
- [10] H. Budzier and G. Gerlach, *Thermal Infrared Sensors: Theory, Optimization and Practice*, Wiley, Chapter 6, 2011.
- [11] A. W. M. Lee and Q. Hu, “Real-time, continuous-wave terahertz imaging by use of a microbolometer focal-plane array,” *Opt. Lett.*, vol. 30, no. 19, pp. 2563–2565, 2005.
- [12] A. W. M. Lee et al., “Real-time imaging using a 4.3-THz quantum cascade laser and a 320x240 microbolometer focal-plane array,” *IEEE Photon. Technol. Lett.*, vol. 18, no. 13, pp. 1415–1417, 2006.

- [13] B. N. Behnken et al., “Detection of 3.4 THz radiation from a quantum cascade laser using a microbolometer infrared camera,” *Proc. SPIE 6549*, p. 65490C-7, 2007.
- [14] G. L. Carr et al., “High-power terahertz radiation from relativistic electrons,” *Nature*, vol. 420, no. 6912, pp. 153–156, 2002.
- [15] B. S. Williams, “Terahertz quantum-cascade lasers,” *Nat. Phot.*, vol. 1, no. 9, pp. 517–525, 2007.
- [16] S. Kumar, “Recent progress in terahertz quantum cascade lasers,” *IEEE J. Sel. Top. Quantum Electron.*, vol. 17, no. 1, pp. 38–47, 2011.
- [17] R. Köhler et al., “Terahertz semiconductor-heterostructure laser,” *Nature*, vol. 417, no. 6885, pp. 156–159, 2002.
- [18] M. Feiginov et al., “Resonant-tunneling-diode oscillators operating at frequencies above 1.1 THz,” *Appl. Phys. Lett.*, vol. 99, no. 23, p. 233506, 2011.
- [19] H. Tanoto et al., “Greatly enhanced continuous-wave terahertz emission by nano-electrodes in a photoconductive photomixer,” *Nat. Phot.*, vol. 6, no. 2, pp. 121–126, 2012.
- [20] F. Alves and G. Karunasiri, private communication, Aug. 2013.
- [21] N. Oda et al., “Detection of terahertz radiation from quantum cascade laser, using vanadium oxide microbolometer focal plane arrays,” *Proc. SPIE 6940*, p. 69402Y-12, 2008.
- [22] Z. Yin and F. W. Smith, “Optical dielectric function and infrared absorption of hydrogenated amorphous silicon nitride films: Experimental results and effective-medium-approximation analysis,” *Phys. Rev. B Condens. Matter*, vol. 42, no. 6, pp. 3666–3675, 1990.
- [23] B. Kearney et al., “Al/SiO_x/Al single and multiband metamaterial absorbers for terahertz sensor applications,” *Opt. Eng.*, vol. 52, no. 1, pp. 013801–013801, 2013.
- [24] F. Alves et al., “Narrowband terahertz emitters using metamaterial films,” *Opt. Expr.*, vol. 20, no. 19, pp. 21025–21032, 2012.
- [25] B. Kearney et al., “Terahertz metamaterial absorbers with an embedded resistive layer,” *Opt. Mat. Expr.*, vol. 3, no. 8, pp. 1020–1025, 2013.
- [26] F. Alves et al., “Bi-material terahertz sensors using metamaterial structures,” *Opt. Expr.*, vol. 20, no. 11, pp. 13256–13271, 2013.

- [27] R. A. Shelby et al., “Experimental Verification of a Negative Index of Refraction,” *Science*, vol. 292, pp. 77–79, 2001.
- [28] X. Zhang and Z. Liu, “Superlenses to overcome the diffraction limit,” *Nature Materials*, vol. 7, pp. 435–441, 2008.
- [29] N. I. Landy et al., “Perfect metamaterial absorber,” *Phys. Rev. Lett.*, vol. 100, no. 20, p. 207402, 2008.
- [30] F. Alves et al., “Strong terahertz absorption using SiO₂/Al based metamaterial structures,” *Appl. Phys. Lett.*, vol. 100, no. 11, p. 111104, 2012.
- [31] F. Alves et al., “MEMS bi-material terahertz sensor with integrated metamaterial absorber,” *Opt. Lett.*, vol. 37, no. 11, pp. 1886–1888, 2012.
- [32] T. Maier and H. Bruckl, “Wavelength-tunable microbolometers with metamaterial absorbers,” *Opt. Lett.*, vol. 34, no. 19, pp. 3012–3014, 2009.
- [33] L. Huang and H. Chen, “Multi-band and polarization insensitive metamaterial absorber,” *PIER*, vol. 113, pp. 103–110, 2011.
- [34] X. Shen et al., “Polarization-independent wide-angle triple-band metamaterial absorber,” *Opt. Expr.*, vol. 19, no. 10, p. 9401, 2011.
- [35] H. Li et al., “Ultrathin multiband gigahertz metamaterial absorbers,” *J. Appl. Phys.*, vol. 110, no. 1, p. 014909, 2011.
- [36] Q.-Y. Wen et al., “Dual band terahertz metamaterial absorber: design, fabrication, and characterization,” *Appl. Phys. Lett.*, vol. 95, no. 24, p. 241111, 2009.
- [37] L. Huang et al., “Experimental demonstration of terahertz metamaterial absorbers with a broad and flat absorption band,” *Opt. Lett.*, vol. 37, no. 2, pp. 154–156, 2012.
- [38] H. Tao et al., “A dual band terahertz metamaterial absorber,” *J. Phys. D: Appl. Phys.*, vol. 43, no. 22, p. 225102, 2010.
- [39] X.-J. He et al., “Dual-band terahertz metamaterial absorber with polarization insensitivity and wide incident angle,” *PIER*, vol. 115, pp. 381–397, 2011.
- [40] Y. Ma et al., “A terahertz polarization insensitive dual band metamaterial absorber,” *Opt. Lett.*, vol. 36, no. 6, pp. 945–947, 2011.
- [41] B. Zhang et al., “Polarization-independent dual-band infrared perfect absorber based on a metal-dielectric-metal elliptical nanodisk array,” *Opt. Expr.*, vol. 19, no. 16, p. 15221, 2011.

- [42] X. Liu et al., “Taming the blackbody with infrared metamaterials as selective thermal emitters,” *Phys. Rev. Lett.*, vol. 107, no. 4, p. 045901, 2011.
- [43] J. Hao et al., “Nearly total absorption of light and heat generation by plasmonic metamaterials,” *Phys. Rev. B*, vol. 83, no. 16, p. 165107, 2011.
- [44] Y. Todorov et al., “Optical properties of metal-dielectric-metal microcavities in the THz frequency range,” *Opt. Expr.*, vol. 18, no. 13, p. 13886, 2010.
- [45] H.-T. Chen, “Interference theory of metamaterial perfect absorbers,” *Opt. Expr.*, vol. 20, no. 7, pp. 7165–7172, 2012.
- [46] Q.-Y. Wen et al., “Transmission line model and fields analysis of metamaterial absorber in the terahertz band,” *Opt. Expr.*, vol. 17, no. 22, pp. 20256–20265, 2009.
- [47] “Perfectly Matched Layers (PMLs),” COMSOL 4.3 Help Documentation.
- [48] N. Laman and D. Grischkowsky, “Terahertz conductivity of thin metal films,” *Appl. Phys. Lett.*, vol. 93, no. 5, p. 051105, 2008.
- [49] F. Alves et al., “Highly absorbing nano-scale metal films for terahertz applications,” *Opt. Eng.*, vol. 51, no. 6, p. 063801, 2012.
- [50] G. Kirchhoff, “On the relation between the radiating and the absorbing powers of different bodies for light and heat,” *Philos. Mag.*, vol. 20, pp. 1–21, 1860.
- [51] J. M. Palmer and B. G. Grant, “The Art of Radiometry,” SPIE Press, 2010.
- [52] Z. Djuric et al., “A new approach to IR bimaterial detectors theory,” *Infrared Phys. Technol.*, vol. 50, no. 1, pp. 51–57, 2007.
- [53] P. G. Datskos et al., “Performance of uncooled microcantilever thermal detectors,” *Rev. Sci. Instrum.*, vol. 75, no. 4, pp. 1134–1148, 2004.
- [54] E. L. Dereniak and G. D. Boreman, *Infrared Detectors and Systems*, Wiley, 1996.
- [55] P. W. Kruse, *Uncooled Thermal Imaging: Arrays Systems and Applications*, SPIE Press, 2002.
- [56] S. Timoshenko, “Analysis of bi-metal thermostat,” *J. Opt. Soc. Am.*, vol. 11, no. 3, pp. 233–255, 1925.
- [57] Z. Y. Hu et al., “Investigation of adsorption and absorption-induced stresses using microcantilever sensors,” *J. Appl. Phys.*, vol. 90, no. 1, pp. 427–431, 2001.
- [58] D. Grbovic et al., “Arrays of SiO₂ substrate-free micromechanical uncooled infrared and terahertz detectors,” *J. Appl. Phys.*, vol. 104, no. 5, p. 054508, 2008.

- [59] R. Kitamura et al., “Optical constants of silica glass from extreme ultraviolet to far infrared at near room temperature,” *App. Opt.* vol. 46, no. 33, pp. 8118–8133, 2007.
- [60] D. Briggs, Center for Nanophase Materials Sciences, Oak Ridge National Laboratory, Oak Ridge, TN, 37831, personal comm. with Dr. Fabio Alves, 2012.
- [61] S. Fatholouloumi et al., “Thermal behavior investigation of terahertz quantum-cascade lasers,” *IEEE J. Quantum Electron.*, vol. 44, no. 12, pp. 1139–1144, 2008.
- [62] Q. Zhang et al., “Optical readout uncooled infrared imaging detector using knife-edge filter operation,” *Optoelec. Lett.*, vol. 3, no. 2, pp. 119–122, 2007.
- [63] T. Cheng et al., “Optical readout sensitivity of deformed microreflector for uncooled infrared detector: theoretical model and experimental validation,” *J. Opt. Soc. Am. A*, vol. 26, no. 11, pp. 2353–2361, 2009.
- [64] B. N. Behnken et al., “Real-time imaging using a 2.8 THz quantum cascade laser and uncooled infrared microbolometer camera,” *Opt. Lett.*, vol. 33, no. 5, pp. 440–442, 2008.
- [65] T. Maier and H. Brueckl, “Multispectral microbolometers for the midinfrared,” *Opt. Lett.*, vol. 35, no. 22, pp. 3766–3768, 2010.

THIS PAGE INTENTIONALLY LEFT BLANK

INITIAL DISTRIBUTION LIST

1. Defense Technical Information Center
Ft. Belvoir, Virginia
2. Dudley Knox Library
Naval Postgraduate School
Monterey, California